

# Discretization-independent multifidelity operator learning for partial differential equations

Jacob Hauck\* and Yanzhi Zhang†

## Abstract

We develop a new and general encode-approximate-reconstruct operator learning model that leverages learned neural representations of bases for input and output function distributions. We introduce the concepts of *numerical operator learning* and *discretization independence*, which clarify the relationship between theoretical formulations and practical realizations of operator learning models. Our model is discretization-independent, making it particularly effective for multifidelity learning. We establish theoretical approximation guarantees, demonstrating uniform universal approximation under strong assumptions on the input functions and statistical approximation under weaker conditions. To our knowledge, this is the first comprehensive study that investigates how discretization independence enables robust and efficient multifidelity operator learning. We validate our method through extensive numerical experiments involving both local and nonlocal PDEs, including time-independent and time-dependent problems. The results show that multifidelity training significantly improves accuracy and computational efficiency. Moreover, multifidelity training further enhances empirical discretization independence.

**Keywords.** Operator learning, discretization independence, multifidelity learning, reduced-order modeling, performance gap, nonlocal PDEs.

## 1 Introduction

Operator learning is a relatively new form of machine learning in which one attempts to learn an operator, in the functional analysis sense, instead of a single function [20, 37]. Such models are usually applied to learning function-to-function mappings in the context of partial differential equations (PDEs), most often the solution operators of PDEs, which map an input function, like an initial condition or coefficient function, to the corresponding solution of the PDE [18]. Operator learning has been applied to many scientific and engineering problems, for example to fluid flow in porous media [7] and turbulent flow modeling in fluid mechanics [26], to crack propagation in material science [12], to climate modeling [17], and to multiphase flow in geophysics [39]. Operator learning for solving complex problems is increasing in popularity primarily due to its potential to provide significantly more efficient surrogate solvers that rely only on data (meaning that no knowledge of the underlying system is required) [23].

To be considered true approximations of an operator, models in operator learning should, like traditional numerical methods, have the ability to produce accurate results independent of the discretization used to represent the input and output functions [23]. We will call this property

---

\*Department of Mathematics and Statistics, Missouri University of Science and Technology, Rolla, MO 65409 (Email: jacobhauck@mst.edu)

†Department of Mathematics and Statistics, Missouri University of Science and Technology, Rolla, MO 65409 (Email: zhangyanz@umsystem.edu)

*discretization independence*.<sup>1</sup> An important consequence of discretization independence of operator learning models is that they can handle naturally multifidelity problems, which are characterized by the presence of data with multiple levels of fidelity to the true underlying functions being represented. Most operator learning models, however, have only been applied to high fidelity data. Multifidelity operator learning is important because there is a trade-off between level of fidelity and cost to obtain for data: generally, the higher the fidelity, the greater the accuracy but also the greater the cost to obtain and to use [10]. *Multifidelity learning* reduces the cost of data generation and model training by lowering the fidelity of training data as much as possible without sacrificing accuracy, which is particularly important since operator learning often requires large datasets to be effective. However, optimizing this cost–accuracy tradeoff is largely unstudied in operator learning; we aim to address this gap in this work.

Existing operator learning methods can be broadly classified into three groups according to their overall structure: neural operators [22,23], transformers [5,25], and encode-approximate-reconstruct models [13, 20]. The encode-approximate-reconstruct framework has two main advantages over other approaches: simple structure and well-understood approximation theory [21]. These methods, however, often fail to be discretization independent because some architectural choices depend on a specific representation of the input or output function [4, 14, 28]. For example, DeepONet [28] requires the input function to be sampled on a fixed set of sensor points; more detailed discussion on discretization independence, or lack thereof, for encode-approximate-reconstruct methods is given in Section 3.1. Consequently, these methods currently struggle to handle multifidelity problems. So far a limited number of other methods have attempted to use encode-approximate-reconstruct models for multifidelity learning [8,15,30], but these methods require separate submodels to handle different fidelities, as the underlying models used are not discretization independent. We remark that the idea of discretization independence has been explored for neural operators [18] and transformers [5, 11] in relation to different sampling meshes [23,25], in which they have been shown to be very effective, but the use of discretization independence in these models has not been applied to multifidelity learning.

In this work, we develop a new and general encode-approximate-reconstruct operator learning model that is discretization-independent and inherently enables multifidelity learning (see Figure 1). Our main contributions can be summarized as follows:

- We develop the new concepts of *numerical operator learning* and *discretization independence*. These concepts clarify the relationship between theoretical and practical realizations of operator learning and provide a novel qualitative means of comparing operator learning models in terms of discretization independence, which we demonstrate on several popular models.
- We propose a novel operator learning architecture that learns neural representations of bases for input and output function distributions. We prove theoretical approximation guarantees for our method, demonstrating universal approximation in a uniform sense, under strong assumptions on the input functions, and in a statistical sense, under weaker assumptions. Our method has significantly better discretization independence compared to existing approaches.
- Our method enables the seamless integration of data representations with variable fidelity through the explicit handling of different discretizations, making it particularly effective for multifidelity learning. We conduct the first detailed study on how discretization independence facilitates multifidelity operator learning and validate it through extensive experiments.

---

<sup>1</sup>Although some ideas have been proposed [2, 18] to define discretization independence mathematically, there is still a lack of consensus; although, it is generally agreed that some form of discretization independence distinguishes operator learning from other machine learning methods.

Our experiments verify the discretization independence of our method. Furthermore, we demonstrate that multifidelity training can reduce some types of error caused by low-fidelity training data, enabling faster training with lower-fidelity, and therefore less expensive, datasets. Moreover, our experiments show that multifidelity training can further improve empirical discretization independence.

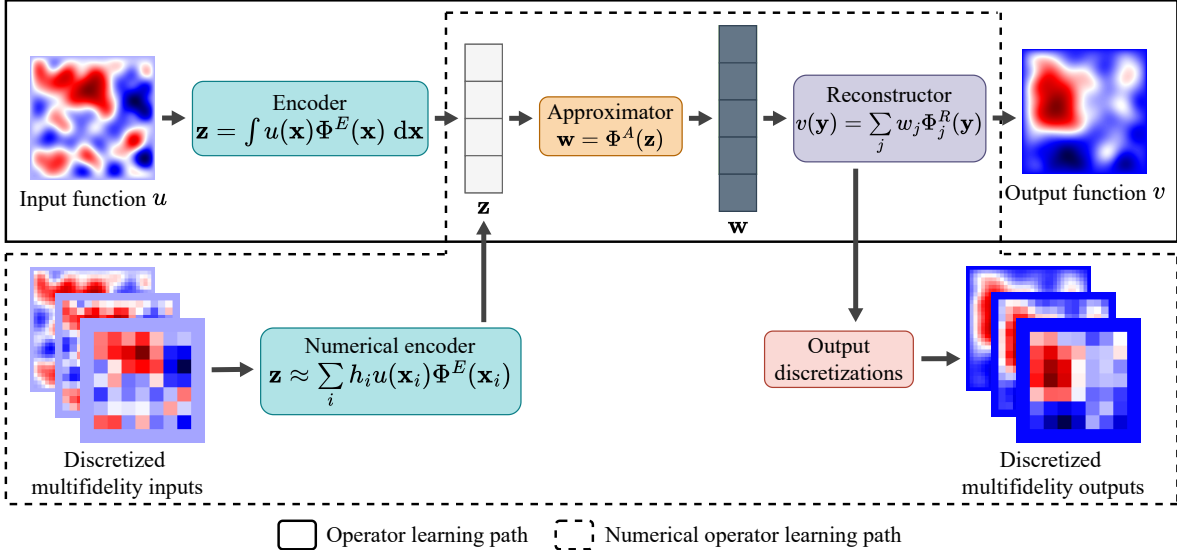


Figure 1: Diagram of the proposed operator learning model.

This paper is organized as follows. In Section 2 we introduce operator learning and present a more general concept of discretization independence. In Section 3 we describe our new method, demonstrate its discretization independence properties, prove approximation theorems, and show that other encode-approximate-reconstruct have limited discretization independence in comparison. In Section 4 we perform numerical experiments that verify discretization independence of our method in practice and also provide insights into issues with single-fidelity learning and benefits of multifidelity learning using our model. Finally, in Section 5 we provide some concluding remarks and discussion.

## 2 Background and related work

In this section we establish the main concepts of operator learning and discuss its fundamental properties. Specifically, we introduce our novel concept of *numerical operator learning*. We also provide a brief review and discussion of the key ideas and limitations underlying existing operator learning approaches.

### 2.1 Operator learning

We start by providing a precise definition of operator learning (in the supervised learning paradigm), which will require fairly complex notation; see Appendix A for a comprehensive list. Let  $\mathcal{U}$  and  $\mathcal{V}$  be infinite-dimensional vector spaces, and let  $G^\dagger : \mathcal{U} \rightarrow \mathcal{V}$  denote an operator mapping the input space  $\mathcal{U}$  to the output space  $\mathcal{V}$ . Suppose that we can collect data  $u^{(i)} \in \mathcal{U}$  and  $v^{(i)} \in \mathcal{V}$  that satisfy  $v^{(i)} = G^\dagger(u^{(i)})$  for  $i = 1, 2, \dots, N$ . The objective of operator learning is to learn an approximation

of  $G^\dagger$  from the dataset  $\{(u^{(i)}, v^{(i)})\}_{i=1}^N$ . The data points  $u^{(i)} \in \mathcal{U}$  and  $v^{(i)} \in \mathcal{V}$  are, in general, infinite-dimensional.

By contrast, in machine learning the data points consist of finite-dimensional vectors, and one uses the data to approximate a function  $g : \mathbb{R}^m \rightarrow \mathbb{R}^n$ , rather than an operator. Operator learning can, therefore, be viewed as a generalization of machine learning, in which the domain and codomain of  $g$  are allowed to be more general vector spaces than  $\mathbb{R}^m$  and  $\mathbb{R}^n$ , mirroring the generalization of a linear transformation in linear algebra to a linear operator in functional analysis. We now present a formal definition of operator learning within the supervised learning paradigm.

**Definition 2.1** (Supervised Operator Learning). *Let  $\mathcal{U}$  and  $\mathcal{V}$  be (infinite-dimensional) vector spaces, and let  $G^\dagger : \mathcal{U} \rightarrow \mathcal{V}$  be an operator. An operator learning model is a parametric operator  $G_\theta : \mathcal{U} \rightarrow \mathcal{V}$  depending on the model parameter vector  $\theta \in \mathbb{R}^P$ . Given a dataset  $\{(u^{(i)}, v^{(i)})\}_{i=1}^N$ , where  $u^{(i)} \in \mathcal{U}$ ,  $v^{(i)} \in \mathcal{V}$ , and  $v^{(i)} = G^\dagger(u^{(i)})$ , the model  $G_\theta$  is trained to approximate  $G^\dagger$  by minimizing the empirical risk  $\mathcal{R} : \mathbb{R}^P \rightarrow \mathbb{R}$  with respect to  $\theta$ , i.e.,*

$$\theta^* = \underset{\theta}{\operatorname{argmin}} \mathcal{R}(\theta), \quad \text{with } \mathcal{R}(\theta) = \frac{1}{N} \sum_{i=1}^N L(G_\theta(u^{(i)}), v^{(i)}), \quad (2.1)$$

where  $L : \mathcal{V} \times \mathcal{V} \rightarrow \mathbb{R}$ , called the loss functional, is a functional measuring the error between  $G_\theta(u^{(i)})$  and  $v^{(i)} = G^\dagger(u^{(i)})$ .

Theoretically, this formulation is superficially very similar to supervised machine learning. Computationally, however, a data point  $(u^{(i)}, v^{(i)})$  must be represented by a pair of finite-dimensional vectors  $(\mathbf{u}^{(i)}, \mathbf{v}^{(i)})$ , where  $\mathbf{u}^{(i)} \in \mathbb{R}^{m_i}$  and  $\mathbf{v}^{(i)} \in \mathbb{R}^{n_i}$  are discrete representations of the true, infinite-dimensional data  $u^{(i)} \in \mathcal{U}$  and  $v^{(i)} \in \mathcal{V}$ . Note that  $m_i \neq n_i$ , so that the representations of  $u^{(i)}$  and  $v^{(i)}$  are not necessarily related; moreover, the representations depend on  $i$ , so that each data point may potentially be represented in a different way. Hence, a practical operator learning model must be able to handle different representations of its inputs and outputs. We propose a framework called *numerical operator learning*, in which we account for computational representations explicitly.

The process of representing the infinite-dimensional data  $u^{(i)}$  and  $v^{(i)}$  by finite-dimensional vectors, that is, discretization, is described by mappings called *discretization operators*, which we denote by  $D_U : \mathcal{U} \rightarrow \mathbb{R}^m$  and  $D_V : \mathcal{V} \rightarrow \mathbb{R}^n$ . Then  $(\mathbf{u}^{(i)}, \mathbf{v}^{(i)}) = (D_U^i(u^{(i)}), D_V^i(v^{(i)}))$  is the discrete representation of  $(u^{(i)}, v^{(i)})$ . The approximation of operator learning using these representations consists of approximating the discrete representation  $\mathbf{v}^{(i)} = D_V^i(G_\theta(u^{(i)}))$  of the output of the operator learning model in terms of the discrete representation  $\mathbf{u}^{(i)}$  of the input. One also needs to approximate the loss functional  $L(G_\theta(u^{(i)}), v^{(i)})$  in terms of  $\mathbf{u}^{(i)}$  and  $\mathbf{v}^{(i)}$ . This way, the empirical risk minimization process can be performed using an approximation of the true empirical risk that depends only on the discrete representations of the input and output. This leads us to the following definition of numerical operator learning.

**Definition 2.2** (Supervised Numerical Operator Learning). *Let  $\mathcal{U}$  and  $\mathcal{V}$  be (infinite-dimensional) vector spaces, and let  $G^\dagger : \mathcal{U} \rightarrow \mathcal{V}$  be an operator. Let  $\mathcal{D} = \{(D_U^\alpha, D_V^\alpha)\}_\alpha$  be a set of discretizations indexed by a parameter  $\alpha$ , so that  $D_U^\alpha : \mathcal{U} \rightarrow \mathbb{R}^{m_\alpha}$ , and  $D_V^\alpha : \mathcal{V} \rightarrow \mathbb{R}^{n_\alpha}$ . A numerical operator learning model is a parametric mapping  $\tilde{G}_\theta(D_U, D_V; \cdot) : \mathbb{R}^m \rightarrow \mathbb{R}^n$ , provided that there is an operator learning model  $G_\theta$  and a numerical realization  $\ell(D_V; \cdot, \cdot) : \mathbb{R}^n \times \mathbb{R}^n \rightarrow \mathbb{R}$  of the loss functional  $L$  so that*

$$D_V(G_\theta(u)) \approx \tilde{G}_\theta(D_U, D_V; D_U(u)), \quad \ell(D_V; D_V(v), D_V(v')) \approx L(v, v'), \quad (2.2)$$

where  $v, v' \in \mathcal{V}$ . With this, one may approximately solve the empirical risk minimization in (2.1) by minimizing the numerical empirical risk  $\tilde{\mathcal{R}}$  to find a numerical optimal parameter  $\tilde{\theta}^* \in \mathbb{R}^P$ :

$$\tilde{\theta}^* = \underset{\theta}{\operatorname{argmin}} \tilde{\mathcal{R}}(\theta), \quad \tilde{\mathcal{R}}(\theta) = \frac{1}{N} \sum_{i=1}^N \ell(D_{\mathcal{V}}^i; \tilde{G}_{\theta}(D_{\mathcal{U}}^i, D_{\mathcal{V}}^i; \mathbf{u}^{(i)}), \mathbf{v}^{(i)}). \quad (2.3)$$

That is,  $\tilde{G}_{\theta}(D_{\mathcal{U}}, D_{\mathcal{V}}; \cdot)$  can be viewed as a numerical realization of the operator model  $G_{\theta}$ .

We remark that for any given  $i$ , and possibly even all  $i$ , we could have  $D_{\mathcal{U}}^i \neq D_{\mathcal{V}}^i$ . Furthermore, for any  $i \neq i'$ , it is possible that  $D_{\mathcal{U}}^i \neq D_{\mathcal{U}}^{i'}$  or  $D_{\mathcal{V}}^i \neq D_{\mathcal{V}}^{i'}$ . Thus, the number and meaning of the components of  $\mathbf{u}^{(i)}$  and  $\mathbf{v}^{(i)}$ , the actual data used computationally, depends on  $i$ . This is the key difference between numerical operator learning and machine learning; a numerical operator learning model must handle  $\mathbf{u}^{(i)}$  and  $\mathbf{v}^{(i)}$  so that it can adapt to different  $D_{\mathcal{U}}^i$  and  $D_{\mathcal{V}}^i$ .

**Discretization independence** The discretizations  $D_{\mathcal{U}}$  and  $D_{\mathcal{V}}$  play a significant role in the design of operator learning models, and vice versa. In fact, every practical method of numerical operator learning works only under some more or less restrictive assumptions about the types of discretizations being used; consequently, we propose the concept of the *effective discretization set*  $\mathcal{D} = \{(D_{\mathcal{U}}^{\alpha}, D_{\mathcal{V}}^{\alpha})\}_{\alpha}$  of an operator learning model, where  $\alpha$  is some indexing parameter. The set  $\mathcal{D}$  consists precisely of those pairs of discretizations under which the approximations in (2.2) hold. There is a lot of freedom in choosing the set  $\mathcal{D}$  of effective discretizations, which allows for the possibility of a numerical operator learning method that works for only one discretization or for only a limited set of discretizations. For example, the Fourier Neural Operator (FNO) [23] relies on using the Fast Fourier Transform (FFT) to approximate efficiently the convolution integrals in the model. The FFT algorithm only works when the input function is discretized by sampling on a uniform grid; as a result, FNO can be applied only when the input and output functions are discretized by sampling on a uniform grid, which can be expressed as a constraint on FNO's effective discretization set  $\mathcal{D}$ .

In this work, we will refer to the (vaguely defined) requirements of (2.2) as *discretization independence* to avoid confusion with either of the more specific ideas proposed. Discretization independence is the defining characteristic of numerical operator learning models, so one could compare models based on how well they achieve this property. To say that a model is more or less discretization independent than another amounts to saying something about the relative sizes of their effective discretization sets. Thus, we have a systematic means of comparing discretization independence for different methods. We will construct the effective discretization sets for the method that we developed as well as for a few other similar methods (see Section 3.1); as we will see, our method has a qualitatively much larger effective discretization set. Naturally, all else being equal, a model with greater discretization independence is more desirable.

We note that the nature of the approximations in (2.2) is left vague on purpose, as it is not fully decided in the literature what the appropriate requirement should be. One idea, called representation equivalence, takes the set of discretizations  $\mathcal{D}$  to be frame-theoretic analysis operators and requires exact equality [2]. Another idea, called discretization invariance, takes the set of discretizations  $\mathcal{D}$  to be sampling operators on different meshes and requires approximate equality with convergence as the mesh becomes finer [18]. Both ideas fit into our framework of numerical operator learning, which can be viewed as a unified formulation. For example, discretization independence in operator learning reduces to representation equivalence if  $\mathcal{U}$  and  $\mathcal{V}$  are chosen to be Hilbert spaces,  $\mathcal{D}$  consists of frame-theoretic analysis operators, and the approximations in (2.2) are taken to be exact equalities. Similarly, discretization independence reduces to discretization invariance if  $\mathcal{U}$  and  $\mathcal{V}$  are taken to be spaces of continuous functions on bounded domains  $\Omega_{\mathcal{U}} \subseteq \mathbb{R}^{d_{\mathcal{U}}}$  and

$\Omega_V \subseteq \mathbb{R}^{d_V}$ , the set  $\mathcal{D}$  consists of sampling discretizations, and the approximation in (2.2) is taken to mean convergence uniformly in  $\mathcal{V}$  as the maximum distance between pairs of distinct sampling points approaches zero.

**Remark 2.1.** Since nearly all operator learning models are formulated to learn mappings between function spaces, we will assume from now on that  $\mathcal{U} \subseteq L^2(\Omega_U)$  and  $\mathcal{V} \subseteq L^2(\Omega_V)$ , where  $\Omega_U \subseteq \mathbb{R}^{d_U}$  and  $\Omega_V \subseteq \mathbb{R}^{d_V}$  are bounded domains. In other words,  $\mathcal{U}$  and  $\mathcal{V}$  are function spaces. We will add further assumptions about  $\mathcal{U}$  and  $\mathcal{V}$  as necessary.

Some problems consider operators on product spaces whose factors are function spaces, that is, operators with multiple inputs or outputs; however, handling multiple inputs and outputs is not the purpose of this work, so we focus on learning operators with a single input function and a single output function.

**Multifidelity learning** Multifidelity data arises naturally when measuring real data because sensor setups may vary, and it also arises naturally when using numerical simulations because most numerical solvers have user-specified parameters that control the discretization, and therefore accuracy, of the solver. The main benefit of multifidelity data is that it can be used to optimize the cost-accuracy tradeoff: whereas low-fidelity data is usually cheap to obtain but reduces accuracy, high-fidelity data is usually expensive to obtain but increases accuracy [15]. Using only low- or high-fidelity data may result in inadequate performance or unacceptable cost, but using the right mixture of fidelities results in adequate performance at the lowest possible cost.

A key challenge in multifidelity learning is to develop a method that can fuse different representations of the same underlying system while accounting for different degrees of fidelity. Numerical operator learning is well-suited to handling this challenge. Suppose that  $u \in \mathcal{U}$  is the true data, and let  $D_U^\ell(u) = \mathbf{u}_\ell \in \mathbb{R}^{m_\ell}$  and  $D_U^h(u) = \mathbf{u}_h \in \mathbb{R}^{m_h}$  denote its low- and high-fidelity representations, respectively. A numerical operator learning model  $\tilde{G}_\theta(D_U, D_V; \cdot)$  automatically handles these different representations by (2.2):

$$\tilde{G}_\theta(D_U^\ell, D_V; \mathbf{u}_\ell) \approx D_V(G_\theta(u)) \approx \tilde{G}_\theta(D_U^h, D_V; \mathbf{u}_h),$$

where  $D_V$  is any output discretization.

In definition 2.2 the key aspect of numerical operator learning that differs from machine learning is the explicit handling of different discretizations. Operator learning handles multifidelity data gracefully because of the explicit treatment of different discretizations; hence, applying operator learning to multifidelity problems highlights its most important strength over machine learning. Therefore, we argue that a good operator learning model should emphasize this difference; although, we note that using the framework of operator learning also provides a conceptual advantage by suggesting the context in which a model should be applied.

## 2.2 Brief review of existing methods

Below we briefly review existing operator learning approaches, focusing on their discretization independence and other key properties. These methods can be broadly classified into three groups according to their overall structure: neural operators [22, 23], transformers [5, 13, 25], and encode-approximate-reconstruct models [13, 20].

Neural operators [18, 22–24] transform an input function through a sequence of functional hidden states by alternating integral transforms and pointwise nonlinear operators. They are formulated at the theoretical level of operator learning but implemented at the practical level of numerical operator learning. This makes the model more interpretable and easier to analyze [19], but more

importantly it means that discretization independence can be achieved by carefully discretizing each component of the model. As a result, neural operators can be applied to any discretizations for which the integral transforms and pointwise nonlinear operators can be approximated. The discretization of neural operators comes with the major challenge of efficiently implementing the general integral transform operator. The most successful neural operator, FNO [23], makes the assumption that the integral transform is a convolution and relies on FFTs to approximate the resulting convolution integrals efficiently. The FFT algorithm, however, only works when the input function is discretized by sampling on a uniform grid, so FNO can be applied only when the input and output functions are discretized by sampling on a uniform grid. So far, there has been some work applying neural operators to multifidelity data [38], but none has directly used the property of discretization independence as we do.

Transformer methods [1, 5, 11, 13, 25, 27, 31] assume the use of a sampling mesh and treat the function samples on the mesh as tokens. Since transformers make use of the attention mechanism from natural language processing, which can handle inputs with different sizes, it follows that transformers can be readily applied to arbitrary sampling meshes, giving them similar discretization independence to neural operators (before additional assumptions that limit discretization independence are made, as in FNO). Transformers offer a very general framework for operator learning due to the flexibility of the attention mechanism; for example, the General Neural Operator Transformer (GNOT) [13] uses attention to handle heterogeneous inputs, such as PDE boundary conditions, vector parameters, and functional parameters. Transformers, however, are formulated directly from the level of numerical operator learning, so most transformers lack a theoretical interpretation. One exception is with Fourier/Galerkin transformers, in which attention is interpreted as a discretization of integral transforms [5], which makes it possible to interpret transformers as a kind of numerical realization of neural operators [18]. To the best of our knowledge, there is no work to date investigating the use of transformers for multifidelity operator learning.

Encode-approximate-reconstruct models are formulated at the level of operator learning in the abstract framework of Lanthaler et al. [21], but, so far, most existing models using this approach have limited discretization independence, with some being applicable only to specific input and output discretizations [4, 14, 28], for example, by applying a neural network directly to function samples [28] or by applying proper orthogonal decomposition for input or output functions at a fixed resolution [4, 14, 29]. In recent works, several strategies have been proposed to improve discretization independence. One encode-approximate-reconstruct model attempts use an attention layer in the encoder to improve discretization independence [33]. Another approach improves discretization independence by incorporating graph neural network [36]. These models, like transformers, are difficult to interpret as operator learning models and lose the theoretical approximation guarantees that earlier models possess. The majority of the work on multifidelity operator learning has been for encode-approximate-reconstruct methods; however, no work has used discretization independence to handle multifidelity data as we do, instead relying on separate sub-models to handle each fidelity level [8, 15, 30].

Compared to neural operator and transformer methods, encode-approximate-reconstruct models are easier to interpret, with a well-developed and general approximation theory [21]. Nevertheless, the most popular models fail to achieve discretization independence comparable to neural operators and transformers. Our main motivation, therefore, is to fill this gap by creating a simple, general encode-approximate-reconstruct model within the framework of operator learning that retains theoretical guarantees and still has as much flexibility as the neural operator and transformer methods in the types of discretizations it can handle. Additionally, we will demonstrate how our model can be trained with multifidelity data, showcasing how multifidelity training can improve accuracy

while decreasing cost.

### 3 Proposed operator learning model

In this section we introduce a novel operator learning model within the encode-approximate-reconstruct framework, present a detailed error analysis of our approach, and highlight its unique properties that distinguish it from existing methods in the same framework. Our model overcomes the limitations of discretization dependence of existing methods [4, 14, 28], and thus provides a more general framework for encode-approximate-reconstruct approaches. Consequently, our model can effectively handle multifidelity data so as to benefit the training and performance of the learned model. Moreover, inherited from the encode-approximate-reconstruct approach, our model can easily handle unstructured data, in contrast to other models, such as FNO [23].

We will start by introducing the encode-approximate-reconstruct framework [21]. It provides a general approach for operator approximation by first encoding the input to a finite-dimensional vector of fixed dimension, then approximating a fixed finite-dimensional representation of the output function, then reconstructing the output function. More precisely, the model  $G_\theta : \mathcal{U} \rightarrow \mathcal{V}$  is decomposed into three components, each of which is a parametric model: an encoder  $E(\theta_E; \cdot) : \mathcal{U} \rightarrow \mathbb{R}^p$ , an approximator  $A(\theta_A; \cdot) : \mathbb{R}^p \rightarrow \mathbb{R}^q$ , and a reconstructor  $R(\theta_R; \cdot) : \mathbb{R}^q \rightarrow \mathcal{V}$ ; the dimensions  $p$  and  $q$  are hyperparameters. Thus, the model  $G_\theta$  is given by

$$G_\theta = R(\theta_R; \cdot) \circ A(\theta_A; \cdot) \circ E(\theta_E; \cdot), \quad (3.1)$$

where the parameter vector  $\theta = (\theta_E, \theta_A, \theta_R)$ . It provides a general framework with the theoretical advantages that the total model error can be analyzed by examining the properties of each component  $E$ ,  $A$ , and  $R$  in isolation.

Following Lanthaler et al. [21] we assume that both the encoder and the reconstructor are linear mappings. By the Riesz representation theorem, linear mappings between the Hilbert space  $L^2$  and a finite-dimensional space can be uniquely determined by a finite set of basis functions in  $L^2$ . Therefore, we propose to approximate the most general class of linear encoders and reconstructors by using neural networks to represent their associated basis functions. Next, we describe the encoder, decoder, and approximator of our model, and then we discretize the resulting operator learning framework into a numerical model, following a paradigm similar to that of neural operators [18].

**Linear encoder** As assumed in Remark 2.1, let  $\mathcal{U}$  be a subspace of  $L^2(\Omega_U)$ . Note that an arbitrary linear mapping  $\psi : \mathcal{U} \rightarrow \mathbb{R}^p$  is given by  $\psi = (\psi_1, \dots, \psi_p)^T$ , where  $\psi_j : \mathcal{U} \rightarrow \mathbb{R}$  is a linear functional on  $\mathcal{U}$  for  $j = 1, 2, \dots, p$ . By the Riesz representation theorem, there exists  $f_j \in L^2(\Omega_U)$  such that  $\psi_j$  can be expressed as an inner product with  $f_j$ , or

$$\psi_j(u) = \langle f_j, u \rangle, \quad j = 1, \dots, p.$$

We propose to approximate the functions  $\{f_j\}_{j=1}^p$  by a neural network  $\Phi^E : \mathbb{R}^{d_U} \rightarrow \mathbb{R}^p$ . Thus, we formulate our linear encoder model  $E(\theta_E; \cdot) : \mathcal{U} \rightarrow \mathbb{R}^p$  as:

$$E_j(\theta_E; u) = \langle \Phi_j^E, u \rangle = \int_{\Omega_U} \Phi_j^E u, \quad j = 1, \dots, p, \quad (3.2)$$

where  $E_j$  and  $\Phi_j^E$  are the  $j$ th components of the vector-valued functions  $E$  and  $\Phi^E$ , respectively. The parameters  $\theta_E$  of the encoder are the parameters of the neural network  $\Phi^E$ . Note that the

only part that requires discretization is the integral in (3.2), thus placing the responsibility for discretization independence on the numerical integration, as is done in neural operators [18].

**Linear reconstructor** Note that any linear mapping  $\varphi : \mathbb{R}^q \rightarrow \mathcal{V}$  can be represented by using the input as the coefficients in a linear combination of elements of  $\mathcal{V}$ . That is, there exist  $g_1, \dots, g_q \in \mathcal{V}$  such that

$$\varphi(\mathbf{w}) = \sum_{j=1}^q w_j g_j, \quad (3.3)$$

where  $w_j$  is the  $j$ th component of  $\mathbf{w} \in \mathbb{R}^q$ . Similar to the encoder basis, we use a neural network  $\Phi^R : \mathbb{R}^{d_V} \rightarrow \mathbb{R}^q$  to approximate the reconstruction basis  $\{g_j\}_{j=1}^q$ . Then we can formulate our reconstructor  $R$  as

$$R(\theta_R; \mathbf{w}) = \sum_{j=1}^q w_j \Phi_j^R, \quad (3.4)$$

where  $\Phi_j^R$  is the  $j$ th component to the vector-valued function  $\Phi^R$ , and  $\theta_R$  are the parameters of  $\Phi^R$ . Note that discretization is essentially not an issue for the reconstructor, since the formula for  $R$  explicitly defines a function in  $\mathcal{V}$  using the finite set of parameters from the neural network  $\Phi^R$ . As a result, the output of  $R$  can, in principle, be discretized in any desired manner, although some discretization strategies require more work than others. For example, evaluating the output function on a sampling mesh is fairly straightforward, whereas projection onto a basis, though not conceptually difficult, requires additional computation.

**Approximator** For the approximator, we only need to model a mapping from  $\mathbb{R}^p$  to  $\mathbb{R}^q$ . Since no discretization is required, we simply define the approximator as  $A = \Phi^A$ , where  $\Phi^A$  is another neural network.

Combining these three components, we obtain our parametric operator

$$G_{\text{ours}} = (R \circ A \circ E) : \mathcal{U} \rightarrow \mathcal{V} \quad (3.5)$$

where our encoder  $E$ , approximator  $A$ , and reconstructor  $R$  are defined as

$$\begin{cases} E(\theta_E; u) = (\langle \Phi_1^E, u \rangle, \dots, \langle \Phi_p^E, u \rangle) \in \mathbb{R}^p, & u \in \mathcal{U}, \\ A(\theta_A; \mathbf{z}) = \Phi^A(\mathbf{z}) \in \mathbb{R}^q, & \mathbf{z} \in \mathbb{R}^p, \\ R(\theta_R; \mathbf{w}) = \sum_{j=1}^q w_j \Phi_j^R \in \mathcal{V}, & \mathbf{w} \in \mathbb{R}^q, \end{cases} \quad (3.6)$$

where  $\Phi^E = (\Phi_1^E, \dots, \Phi_p^E)$ ,  $\Phi^R = (\Phi_1^R, \dots, \Phi_q^R)$ , and  $\mathbf{w} = (w_1, \dots, w_q)$ .

### 3.1 Discretization independence and comparison

As previously discussed, the discretizations  $D_U$  and  $D_V$  play an important role in numerical operator learning models. Hence, before we can define a numerical approximation of our model, we need to determine the set  $\mathcal{D}$  of discretizations to which it will be applied. In our model (3.6), the reconstructor can essentially be used with any output discretization, since the output of our model explicitly defines a function using a finite number of parameters  $\theta_R$ . However, the input relies on the computation of the inner product

$$\langle \Phi_j^E, u \rangle = \int_{\Omega_u} \Phi_j^E u, \quad 1 \leq j \leq p. \quad (3.7)$$

Given that  $\Phi_j^E$  is an explicitly known function (a neural network), the approximation of the inner product in (3.7) depends only on whether it can be accurately evaluated from the discrete representation  $D_U(u)$ .

Let  $\mathcal{D}_I$  be the set of discretizations  $D_U : \mathcal{U} \rightarrow \mathbb{R}^m$  for which a numerical quadrature rule  $I(\phi, \cdot)$  exists to approximate  $\langle \phi, u \rangle$  for a given function  $\phi$ , that is,

$$\langle \phi, u \rangle \approx I(\phi, D_U(u)), \quad \text{for all } u \in \mathcal{U}.$$

Then our model can be applied numerically for the set of discretizations

$$\mathcal{D} = \{(D_U, D_V) : D_U \in \mathcal{D}_I\} \tag{3.8}$$

and our numerical model  $\tilde{G}_\theta$  is given by

$$\tilde{G}_\theta(D_U, D_V; D_U(u)) = R \circ A \circ \tilde{E}(D_U; \cdot), \tag{3.9}$$

where the numerical encoder  $\tilde{E}(D_U; \cdot)$  is given by

$$\tilde{E}(D_U; \mathbf{u}) = (I(\Phi_1^E, \mathbf{u}), I(\Phi_2^E, \mathbf{u}), \dots, I(\Phi_p^E, \mathbf{u})), \quad \mathbf{u} \in \mathbb{R}^m. \tag{3.10}$$

Thus, our method can effectively handle any input discretization for which numerical integration is feasible and any choice of output discretization. In our experiments, we use the trapezoidal rule for numerical integration, but any numerical quadrature rule can work. Note that the responsibility of maintaining discretization independence in our model is placed on the numerical integration, which is essentially the same strategy used by neural operators [18]. As we will show in our experiments, our model breaks down when the fidelity of the input becomes too low for numerical integration to approximate the inner product integrals accurately (see, in particular, Figure 8).

**Remark 3.1.** The accuracy of the numerical integration  $I(\Phi_j^E, \mathbf{u})$  depends on the resolution of  $\mathbf{u}$  and the choice of quadrature rule. This suggests that using a higher-order quadrature rule could enhance discretization independence by increasing the accuracy of numerical integration for smooth, low-fidelity input functions. This would also allow our model to use lower-fidelity training data, improving data efficiency.

Next, we compare discretization independence of our method and other encode–approximate–reconstruct methods by characterizing their effective discretization sets  $\mathcal{D}$ . Our method can effectively handle arbitrary input and output discretizations, which significantly distinguishes it from DeepONet [28], PCA-Net [4] (also called POD-NN by Hesthaven and Ubbiali [14]), and POD-DeepONet [29]. In contrast, DeepONet is limited to a single input discretization, namely, sampling at a set of predefined sensor points [28]. The same restriction applies to PCA-Net and POD-DeepONet, which additionally require the output discretization to lie on a fixed sampling grid, unless interpolation is employed [4].

To facilitate more detailed comparison, we formulate all models in a unified encode–approximate–reconstruct framework.<sup>2</sup> All methods being compared rely on sampling discretization in some way; therefore, we develop the following notation to describe their effective discretization sets. Let  $\mathcal{D}_S$  and  $\mathcal{D}_Q$  denote sets of input and output discretizations that can provide sample function values on the point sets  $S = \{\mathbf{x}_j\}_{j=1}^m \subseteq \Omega_U$  and  $Q = \{\mathbf{y}_j\}_{j=1}^n \subseteq \Omega_V$ . That is,  $D_U \in \mathcal{D}_S$  if and only if there exists a mapping  $\pi_S$  such that  $\pi_S(D_U(u)) = (u(\mathbf{x}_1), \dots, u(\mathbf{x}_m))^T$  for all  $u \in \mathcal{U}$ ; membership in  $\mathcal{D}_Q$  requires the existence of an analogous mapping  $\pi_Q$ . The main differences between methods lie in the numerical treatment of the encoder and reconstructor; see Table 1.

<sup>2</sup>This is not how these (i.e., DeepONet, PCA-Net, POD-NN, and POD-DeepONet) methods were originally formulated, but presenting them in this way makes it easier to compare with ours.

Method	Numerical model $\tilde{G}_\theta$	Approximation of $E$ or $R$	DI condition
<b>Ours</b>	$R \circ A \circ \tilde{E}(D_U; \cdot)$	$\tilde{E}(D_U; \mathbf{u}) = (I(\Phi_1^E, \mathbf{u}), \dots, I(\Phi_p^E, \mathbf{u}))$	<b>None</b>
DeepONet		$\tilde{E}(D_U; \mathbf{u}) = (u(\mathbf{x}_1), \dots, u(\mathbf{x}_p))$	$D_U \in \mathcal{D}_S$
POD-DeepONet	$\tilde{R}(D_V; \cdot) \circ A \circ \tilde{E}(D_U; \cdot)$	$\tilde{E}(D_U; \mathbf{u}) = (u(\mathbf{x}_1), \dots, u(\mathbf{x}_p))$ $\tilde{R}(D_V; \mathbf{w}) = \pi_V \left( \mathbf{f}_0 + \sum_{j=1}^q w_j \mathbf{f}_j \right)$	$D_U \in \mathcal{D}_S$ $D_V \in \mathcal{D}_Q$
PCA-Net		$\tilde{E}(D_U; \mathbf{u}) = (\mathbf{g}_1^T \pi_S(\mathbf{u}), \dots, \mathbf{g}_p^T \pi_S(\mathbf{u}))$ $\tilde{R}(D_V; \mathbf{w}) = \pi_Q \left( \sum_{j=1}^q w_j \mathbf{f}_j \right)$	$D_U \in \mathcal{D}_S$ $D_V \in \mathcal{D}_Q$

Table 1: Comparison of our method and those from DeepONet, PCA-Net/POD-NN and POD-DeepONet, for their numerical models and their discretization independence (DI) condition. For POD/PCA methods, the values  $\{w_j\}_{j=1}^q$  are the coefficients predicted by the approximator.

The encoder of DeepONet is given by sampling on the set  $S$ . Then the numerical encoder  $\tilde{E}$  of DeepONet is simply given by  $\pi_S$ . The POD-DeepONet [29] model uses the same numerical encoder as DeepONet, but further approximates the reconstructor using a set of basis functions  $\{g_\ell\}_{\ell=1}^q$  obtained via proper orthogonal decomposition (POD) applied to the output functions  $\{v^{(i)}\}_{i=1}^N$  in the training data. It assumes that the discretized function data provide the sample values on the points in  $Q$ ; that is,  $D_V^i \in \mathcal{D}_Q$  for  $i = 1, 2, \dots, N$ . Numerically, POD is implemented by performing principal component analysis on the samples of the input functions on  $Q$ , yielding a set of vectors  $\{\mathbf{g}_\ell\}_{\ell=1}^q$  that approximate the sample values on  $Q$  of the true POD basis functions  $\{g_\ell\}_{\ell=1}^q$ . In other words, POD-DeepONet can evaluate the output function only at the points  $Q$ , as the POD basis functions are known only at those points. Consequently, in addition to assuming that functions in  $\mathcal{U}$  are defined at the points  $S$ , we must also assume that functions in  $\mathcal{V}$  are well-defined at the points  $Q$ .

PCA-Net [4, 14] uses POD for both the encoder and reconstructor, where  $S$  and  $Q$  are used as the sampling points for the numerical implementation of POD for the input and output functions. Thus, one obtains the vectors  $\{\mathbf{f}_k\}_{k=1}^p$ , which give the approximate sample values of  $\{f_k\}_{k=1}^p$ , the POD basis functions for the input. This makes PCA-Net essentially as discretization dependent as POD-DeepONet. We note that the independence in POD-DeepONet and PCA-Net is only approximate, as the vectors  $\mathbf{g}_\ell$  and  $\mathbf{f}_k$  only approximate the functions  $g_\ell$  and  $f_k$ .

**Remark 3.2.** DeepONet cannot approximate the optimal linear encoder of fixed dimension  $p$  to an arbitrary degree of accuracy. It can, in a probabilistic sense with randomly chosen sensors, achieve optimal accuracy asymptotically (see Theorem 3.7 of Lanthaler et al. [21]), but it cannot approach the optimal encoding error for a linear encoder with any fixed dimension  $p$ . In PCA-Net the encoder is already given by projection onto the optimal subspace of dimension  $p$  (or an approximation thereof, at least) due to the optimality of POD; however, the method has very strict discretization dependence. Our model maintains the optimality properties of PCA-Net and at the same time is discretization independent.

**Remark 3.3.** Considering sampling discretizations adds the requirement that the input and output functions be defined at the sampling points, which is a strong assumption for functions in  $\mathcal{U} \subseteq L^2(\Omega_U)$ , as functions in  $L^2$  are not necessarily defined pointwise.

Finally, we remark that requiring the input and/or output functions to be known at specific

sets of points significantly limits the flexibility of DeepONet, POD-DeepONet, and PCA-Net. In particular, this constraint often makes multifidelity learning infeasible for these methods unless substantial modifications are made, such as using multiple model instances to handle different fidelity levels, as proposed in [8, 15, 30].

### 3.2 Approximation theory

In this section, we present two theorems that establish the universal approximation capabilities of our method, building on results from the encode-approximate-reconstruct framework [21]. The first theorem shows that our method can uniformly approximate continuous operators on compact domains. The second theorem, combined with existing results, demonstrates that our method can approximate Lipschitz continuous operators in a statistical sense, for any distribution over the input functions.

The first theorem builds on the theoretical operator learning architecture proposed by Chen and Chen [6], which is restated below for clarity and completeness.

**Theorem 3.1.** (Chen and Chen [6]) *Let  $\mathcal{X}$  be a Banach space, and let  $\Omega_U \subseteq \mathcal{X}$  and  $\Omega_V \subseteq \mathbb{R}^{d_V}$ . Let  $\mathcal{U} \subseteq C(\Omega_U)$  be compact sets, and  $\mathcal{V} = C(\Omega_V)$ . Suppose that  $G^\dagger : \mathcal{U} \rightarrow \mathcal{V}$  is continuous (with respect to the  $C(\Omega_U)$  and  $C(\Omega_V)$  topologies). Then for any  $\varepsilon > 0$ , there exists a set of points  $\{\mathbf{x}_j\}_{j=1}^m \subseteq \Omega_U$  and one-layer neural networks<sup>3</sup>  $B : \mathbb{R}^m \rightarrow \mathbb{R}^p$  and  $T : \mathbb{R}^{d_V} \rightarrow \mathbb{R}^p$  such that*

$$|G^\dagger(u)(\mathbf{y}) - B(\mathbf{u}) \cdot T(\mathbf{y})| < \varepsilon \quad (3.11)$$

for all  $u \in \mathcal{U}$  and all  $\mathbf{y} \in \Omega_V$ , where  $\mathbf{u} = \{u(\mathbf{x}_j)\}_{j=1}^m$ .

Next, we provide the uniform approximation theorem for our method.

**Theorem 3.2.** *Consider the same setting<sup>4</sup> as in Theorem 3.1. Then for any  $\varepsilon > 0$ , there exists a model  $G_{\text{ours}}$  such that*

$$|G^\dagger(u)(\mathbf{y}) - G_{\text{ours}}(u)(\mathbf{y})| < \varepsilon \quad (3.12)$$

for all  $u \in \mathcal{U}$  and all  $\mathbf{y} \in \Omega_V$ .

*Proof.* The proof can be done by applying Theorem 3.1. To this end, we construct our model  $G_{\text{ours}}$  by letting  $\Phi^A = B$  and  $\Phi^R = T$  along with sample points  $\{\mathbf{x}_j\}_{j=1}^m \subseteq \Omega_U$  satisfying (3.11), the approximation condition from the theorem. Then, we need only use  $\Phi^E$  to approximate the sampling operator  $u \mapsto \{u(\mathbf{x}_j)\} = \mathbf{u}$ .

For each  $j = 1, 2, \dots, m$ , we choose a function  $f_j$  that satisfies  $\langle f_j, u \rangle \approx u(\mathbf{x}_j)$  and can be approximated by a neural network  $\Phi_j^E$ ; that is, for any  $\varepsilon_1 > 0$ , there is a neural network  $\Phi_j^E$  such that

$$\|\Phi_j^E - f_j\|_{L^1(\Omega_U)} < \varepsilon_1, \quad j = 1, 2, \dots, m. \quad (3.13)$$

Here, we take  $f_j$  to be approximately a Dirac delta function. Specifically,  $f_j$  is nonnegative, supported in a small neighborhood of  $\mathbf{x}_j$ , and has integral equal to 1.

<sup>3</sup>The original formulation in [6] does not explicitly use the language of neural networks, but presents an equivalent constructive result. For clarity, we have modified the statement. Note that the activation function in the two neural networks should be the same and must be a Tauber-Wiener function, which includes all commonly used activation functions.

<sup>4</sup>Almost the same, except for the minor additional requirement that the activation functions in the approximator/branch network are continuous.

The size of the neighborhood  $B(\mathbf{x}_j)$  depends on how quickly functions in  $\mathcal{U}$  can change. Since  $\mathcal{U}$  is a compact subset of  $C(\Omega_U)$ , for any  $\varepsilon_2 > 0$ , there exists a finite set of functions  $\{g_\ell\}_{\ell=1}^L \subseteq \mathcal{U}$  such that for every  $u \in \mathcal{U}$ , there exists a  $g_\ell$  satisfying

$$\|u - g_\ell\|_{C(\Omega_U)} = \sup_{\mathbf{x} \in \Omega_U} |u(\mathbf{x}) - g_\ell(\mathbf{x})| < \varepsilon_2. \quad (3.14)$$

Furthermore, since each  $g_\ell$  is continuous, for any  $\varepsilon_3 > 0$ , we can choose a radius  $r > 0$  such that

$$|g_\ell(\mathbf{x}) - g_k(\mathbf{x}_j)| < \varepsilon_3, \quad (3.15)$$

for all  $\ell, k = 1, 2, \dots, L$ , and all  $\mathbf{x} \in \Omega_U$  satisfying  $|\mathbf{x} - \mathbf{x}_j| < r$ . Eqs. (3.14) and (3.15) implies that all functions in  $\mathcal{U}$  are close to one of the  $g_\ell$ , and the radius  $r$  controls all functions  $g_\ell$ . It immediately follows that the radius  $r$  controls how quickly all functions in  $\mathcal{U}$  change.

Thus, we choose the support of  $f_j$  to be  $B(\mathbf{x}_j) = \{\mathbf{x} \in \Omega_U : |\mathbf{x} - \mathbf{x}_j| < r\}$ . Then we obtain

$$\begin{aligned} |u(\mathbf{x}_j) - \langle \Phi_j^E, u \rangle| &= \left| \int_{\Omega_U} (u(\mathbf{x}_j) f_j(\mathbf{x}) - u(\mathbf{x}) \Phi_j^E(\mathbf{x})) \, d\mathbf{x} \right| \\ &\leq \|u\|_{C(\Omega_U)} \|f_j - \Phi_j^E\|_{L^1(\Omega_U)} + \left| \int_{B(\mathbf{x}_j)} (u(\mathbf{x}_j) - u(\mathbf{x})) f_j(\mathbf{x}) \, d\mathbf{x} \right| \\ &\leq \varepsilon_1 \|u\|_{C(\Omega_U)} + \int_{B(\mathbf{x}_j)} (|u(\mathbf{x}_j) - g_\ell(\mathbf{x}_j)| + |g_k(\mathbf{x}) - u(\mathbf{x})| + |g_\ell(\mathbf{x}_j) - g_k(\mathbf{x})|) f_j(\mathbf{x}) \, d\mathbf{x} \\ &\leq \varepsilon_1 \|u\|_{C(\Omega_U)} + 2\varepsilon_2 + \varepsilon_3, \end{aligned}$$

by (3.13)–(3.15) and the fact that the integral of  $f_j$  equals 1. Since  $\varepsilon_1, \varepsilon_2,$  and  $\varepsilon_3$  are arbitrary and there exists a constant  $C$  such that  $\|u\|_{C(\Omega_U)} < C$  for all  $u \in \mathcal{U}$  due to the compactness of  $\mathcal{U}$ , it follows that for any  $\delta > 0$ , we can construct a neural network  $\Phi^E$  such that

$$|u(\mathbf{x}_j) - \langle \Phi_j^E, u \rangle| < \delta, \quad j = 1, 2, \dots, m. \quad (3.16)$$

Then for any  $\delta > 0$ , we can construct a model  $G_{\text{ours}}^\delta$  whose encoder network  $\Phi^E$  satisfies (3.16) and whose approximator neural network is  $\Phi^A = B$  and reconstructor neural network is  $\Phi^R = T$ . Then

$$|G^\dagger(u)(\mathbf{y}) - G_{\text{ours}}^\delta(u)(\mathbf{y})| \leq |G^\dagger(u)(\mathbf{y}) - B(\mathbf{u}) \cdot T(\mathbf{y})| + |(B(\mathbf{u}) - B(\{\langle \Phi_j^E, u \rangle\}_j)) \cdot T(\mathbf{y})|. \quad (3.17)$$

Noticing (3.11), then the claim (3.12) immediately follows by showing that the second term in (3.17) can be arbitrarily small for sufficiently small  $\delta$ . This is, indeed, the case because continuous activation functions imply that  $B$  and  $T$  are continuous on their compact domains  $\Omega_U$  and  $\Omega_V$ . Hence,  $T$  is bounded, and  $B$  is uniformly continuous, so for  $\delta$  sufficiently small, the condition (3.16) implies that the second term can be made arbitrarily small.  $\square$

This approximation result extends to specific discretizations  $D_U$  and  $D_V$  in a way that depends on how accurately  $D_U$  and  $D_V$  discretely approximate  $\mathcal{U}$  and  $\mathcal{V}$  (and also on how accurate numerical integration using  $D_U$  can be). This is an immediate consequence of the continuity of the model with respect to  $u$ , the use of which was already demonstrated in the proof of the theorem.

Given a random input  $u \sim \mu$ , the statistical error  $\mathcal{E}$  of an operator learning model  $G_\theta$  for the Lipschitz continuous operator  $G^\dagger$  is defined as [21]

$$\mathcal{E}^2 = \mathbb{E}_{u \sim \mu} \left[ \|G^\dagger(u) - G_\theta(u)\|_{L^2(\Omega_V)}^2 \right], \quad (3.18)$$

that is, the root mean squared  $L^2$  error of the predicted output. This error can be broken into an *encoding error*  $\mathcal{E}_E$ , an *approximation error*  $\mathcal{E}_A$ , and a *reconstruction error*  $\mathcal{E}_R$ , each of which depends only on the corresponding component of the model, that is, the encoder  $E$ , the approximator  $A$ , and reconstructor  $R$ . In particular, the total error of the model can be bounded by

$$\mathcal{E} \leq C_1 \mathcal{E}_E + C_2 \mathcal{E}_A + \mathcal{E}_R, \quad (3.19)$$

where  $C_1$  and  $C_2$  are constants that depend on  $G^\dagger$  [21]. The approximation error and reconstruction error for our choice of approximator and reconstructor have already been studied. Specifically, when the approximator is a multilayer perceptron, as in our case, standard neural network approximation theorems provide bounds on the approximation error  $\mathcal{E}_A$  [21]. Additionally, for linear reconstructors, as in our case, there are bounds on the reconstruction error  $\mathcal{E}_R$  based on combining the analysis of finite-dimensional approximations of the space  $L^2(\Omega_V)$  with neural network approximation theorems [21]. Hence, to bound the statistical error  $\mathcal{E}$ , we need only consider the encoding error  $\mathcal{E}_E$ , which is defined as follows.

Given a probability measure  $\mu$  on  $\mathcal{U} = L^2(\Omega_U)$  with finite second moments, a linear encoder  $E : \mathcal{U} \rightarrow \mathbb{R}^p$ , and a linear mapping  $D : \mathbb{R}^p \rightarrow \mathcal{U}$  (called the *decoder* in the encode-approximate-reconstruct framework), the encoding error  $\mathcal{E}_E$  is defined by

$$\mathcal{E}_E^2 = \mathbb{E}_{u \sim \mu} \left[ \|D(E(u)) - u\|_{L^2(\Omega_U)}^2 \right]. \quad (3.20)$$

Note that we take  $\mathcal{U} = L^2(\Omega_U)$  in this case instead of  $\mathcal{U}$  being some subspace. This makes sense because we can restrict our input function  $u$  to a subspace by choosing  $\mu$  supported only on that supspace. We work in the context of the Hilbert space  $L^2(\Omega_U)$  because it makes it straightforward to compute error estimates for our inner-product-based encoder.

As Lanthaler et al. remark [21], the encoding error can be broken down into two components:

$$\mathcal{E}_E^2 = \mathcal{E}_{\text{aliasing}}^2 + \sum_{k > p} \lambda_k, \quad (3.21)$$

where  $\{\lambda_k\}$  are the eigenvalues, in decreasing order, corresponding to the orthonormal eigenfunctions in the spectral decomposition of the uncentered covariance operator of  $\mu$ . The second term in (3.21) is independent of the encoder and decoder, and it provides a lower bound on the encoding error with a fixed encoding dimension  $p$  (this bound is also specific to  $\mu$ , that is, the distribution of the input function  $u$ ). The first term,  $\mathcal{E}_{\text{aliasing}}^2$ , depends on the encoder and decoder.

In the following theorem, we show that our method can nearly minimize  $\mathcal{E}_{\text{aliasing}}$  for a fixed  $p$  by choosing the encoder network  $\Phi^E$  sufficiently large.

**Theorem 3.3.** *Let  $\mu$  be a probability measure on  $L^2(\Omega_U)$ , representing the law of a random variable  $u$ . For any  $\varepsilon > 0$  and any positive integer  $p$ , there exists a model  $G_{\text{ours}}$  with encoder network  $\Phi^E : \mathbb{R}^{d_u} \rightarrow \mathbb{R}^p$  (and a suitable decoder) such that the aliasing error  $\mathcal{E}_{\text{aliasing}}$  for  $u$  satisfies*

$$\mathcal{E}_{\text{aliasing}} \leq \varepsilon.$$

*Proof.* Let  $\Gamma$  denote the covariance operator of  $u$ , and let  $\{\phi_k\}$  be the eigenfunctions in the spectral decomposition of  $\Gamma$ , so that

$$\Gamma = \sum_{k=1}^{\infty} \lambda_k (\phi_k \otimes \phi_k), \quad (3.22)$$

where the corresponding eigenvalues  $\{\lambda_k\}$  are given in decreasing order.

Given  $\varepsilon > 0$ , standard universality theorems (such as Theorem 3.2 in [3]) ensure the existence of a neural network  $\Phi^E$  such that  $\|\Phi_k^E - \phi_k\|_{L^2(\Omega_u)} \leq \frac{\varepsilon}{\sigma\sqrt{p}}$  for all  $k = 1, 2, \dots, p$ , where  $\sigma^2$  is the uncentered variance of  $u$ . Choose the linear decoder  $D$  as

$$D(\mathbf{z}) = \sum_{k=1}^p z_k \phi_k, \quad \mathbf{z} \in \mathbb{R}^p. \quad (3.23)$$

Then the encoding error can be computed as

$$\begin{aligned} \mathcal{E}_E^2 &= \int_U \|D(E(u)) - u\|_{L^2(\Omega_u)}^2 \, d\mu(u) \\ &= \int_U \left\| \sum_{k=1}^p \phi_k \langle \Phi_k^E, u \rangle - u \right\|_{L^2(\Omega_u)}^2 \, d\mu(u). \end{aligned}$$

Using the representation of  $u$  in the orthonormal basis formed by  $\{\phi_k\}$ , we have

$$\mathcal{E}_E^2 = \int_U \left\| \sum_{k=1}^p \phi_k (\langle \Phi_k^E, u \rangle - \langle \phi_k, u \rangle) - \sum_{k>p} \phi_k \langle \phi_k, u \rangle \right\|_{L^2(\Omega_u)}^2 \, d\mu(u).$$

By the orthonormality of  $\{\phi_k\}$ , we further obtain

$$\mathcal{E}_E^2 = \sum_{k=1}^p \int_U |\langle \Phi_k^E - \phi_k, u \rangle|^2 \, d\mu(u) + \sum_{k>p} \int_U |\langle \phi_k, u \rangle|^2 \, d\mu(u), \quad (3.24)$$

where the second term is actually just the lower error bound from (3.21) (see Appendix C.10 of Lanthaler et al. [21]). Thus,

$$\begin{aligned} \mathcal{E}_{\text{aliasing}}^2 &= \sum_{k=1}^p \int_U |\langle \Phi_k^E - \phi_k, u \rangle|^2 \, d\mu(u) \\ &= \sum_{k=1}^p \int_U \left| \int_{\Omega_u} (\Phi_k^E(\mathbf{x}) - \phi_k(\mathbf{x})) u(\mathbf{x}) \, d\mathbf{x} \right|^2 \, d\mu(u) \\ &\leq \sum_{k=1}^p \int_U \|u\|_{L^2(\Omega_u)}^2 \|\Phi_k^E - \phi_k\|_{L^2(\Omega_u)}^2 \, d\mu(u) \\ &\leq \varepsilon^2. \end{aligned} \quad (3.25)$$

□

**Remark 3.4.** Note that, unlike our method, the DeepONet can only reduce  $\mathcal{E}_{\text{aliasing}}$  asymptotically as  $p \rightarrow \infty$  [21].

**Remark 3.5.** Since the approximation error  $\mathcal{E}_A$  and reconstruction error  $\mathcal{E}_R$  are depend only on the approximator  $A$  and reconstructor  $R$ , and these errors can be made arbitrarily small for suitable choices of  $A$  and  $R$  [21], it follows from Theorem 3.3 that given  $\varepsilon > 0$ , there exists a model  $G_{\text{ours}}$  for which the statistical error  $\mathcal{E}$  satisfies  $\mathcal{E} < \varepsilon$ .

## 4 Numerical experiments

We now carry out numerical experiments to demonstrate the effectiveness of our method and to explore the benefits and limits of multifidelity learning. We focus on operators arising from diverse PDEs, including one- and two-dimensional, linear and nonlinear, local and nonlocal, and time-dependent and time-independent equations. Numerical experiments show that our method is empirically discretization-independent. Training with low-fidelity data, which is cheaper to obtain and faster to train, is generally preferred; however, lower fidelity can introduce approximation errors. We analyze and categorize these errors in detail. Furthermore, we show that incorporating a small amount of high-resolution data through multifidelity training can effectively mitigate some of these issues. This enables the efficient use of low-fidelity data while maintaining accuracy and reducing computational cost.

**Experimental setup:** Consider continuous input and output functions defined on the  $d$ -dimensional domain  $\bar{\Omega}$ , where  $\Omega = (0, 1)^d$ . We will use the same discretization for any given input-output pair. In the following, we will only consider discretizations given by sampling the functions on a uniform grid over  $\bar{\Omega}$ , including samples at the boundaries. As such, we use the trapezoidal rule for numerical integration. We note that these decisions about domain and discretization are not essential; they merely simplify the experimental design and implementation. Note that any domain, discretization, and quadrature rule can be used with our method as long as numerical integration is possible and sufficiently accurate.

To investigate the effects of multifidelity learning, we generated many datasets numerically for each example problem, varying the combination of discretizations in each dataset. In general, a dataset can be described by the parameters  $N$ ,  $(R_1, \dots, R_M)$ , and  $(p_1, \dots, p_M)$ , where  $N$  is the total number of samples in the dataset,  $M$  is the number of distinct discretizations.  $R_i$  denotes the number of sampling points in one spatial dimension for the  $i$ th discretization (so that the total number of spatial points is  $R_i^d$ ), and  $p_i$  is the proportion of the samples that use the  $i$ th discretization. In our setting, we take the same discretization for both the input and output functions; note that the value  $R_i$  uniquely determines the discretization, so we will use this value to identify discretizations concisely. See Figure 2 for an illustrative example of a multifidelity dataset.

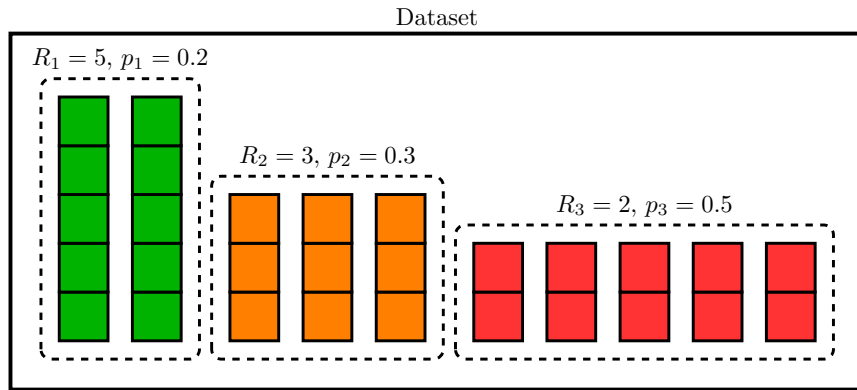


Figure 2: Example of a multifidelity dataset with  $N = 10$  samples and  $M = 3$  fidelity levels.

We implement the neural networks  $\Phi^E$ ,  $\Phi^A$ , and  $\Phi^R$  with multilayer perceptrons with the leaky ReLU activation function, using Fourier feature expansion [29] for  $\Phi^E$  and  $\Phi^R$ . See Appendix B for the training details and model architectures. We train all models on training datasets of size  $N = 2048$  except for the Navier–Stokes models, where we use  $N = 4096$ . The Adam optimization

method with a geometrically attenuated learning rate is used to minimize the  $L^1$  loss<sup>5</sup>, which we approximate by a Riemann sum. All models are tested on single-fidelity ( $M = 1$ ) testing datasets of size  $N = 512$  with varying values of  $R_1$  to assess discretization independence and other multifidelity effects. To evaluate performance we compute the average relative  $L^1$  error (i.e., mean absolute error) between the model prediction and the true output function, again approximate by a Riemann sum. We average errors over multiple training runs with random initial weights for the neural networks  $\Phi^E$ ,  $\Phi^A$ , and  $\Phi^R$  as well as random reorderings of the training dataset.

#### 4.1 Nonlocal Poisson problems

Consider the two-dimensional ( $d = 2$ ) nonlocal Poisson equation with homogeneous Dirichlet boundary conditions:

$$\begin{cases} (-\Delta)^{\frac{\alpha}{2}} u = f(\mathbf{x}), & \mathbf{x} \in \Omega, \\ u(\mathbf{x}) = 0, & \mathbf{x} \in \mathbb{R}^2 \setminus \Omega, \end{cases} \quad (4.1)$$

where the fractional Laplacian  $(-\Delta)^{\frac{\alpha}{2}}$  for  $\alpha \in (0, 2)$  is a nonlocal operator [9, 35]. In our study, we consider the case  $\alpha = 1$ . This operator has numerous applications, including water waves, quantum mechanics, and anomalous diffusion. If  $f$  is continuous on  $\Omega$ , then it is well-known that the function  $u$  is uniquely determined by  $f$  [35]. We define the operator  $G^\dagger$  such that  $u = G^\dagger(f)$ , which is the operator that we attempt to approximate. To obtain a training data point  $(f, u)$ , we generate the input functions  $f$  using a random Fourier series [34], and obtain the corresponding solutions  $u = G^\dagger(f)$  by numerically solving (4.1) at high resolution using the methods described in [40]. Then we downsample both  $f$  and  $u$  to lower resolutions to obtain datasets with various multifidelity parameters.

**Single-fidelity training** We first conduct experiments by training models with only single-fidelity (i.e.  $M = 1$ ) datasets to demonstrate the discretization independence of our method. To this end, all models use the same architecture hyperparameters (described in Appendix B), and training dataset sizes  $N$ , with only the resolution of the training data varying between models. Figures 3 and 4 compare the predicted solutions and their errors from models with different training data resolution ( $R_1$ ) values. In Figure 3, the test input data has the same resolution as the training data, while in Figure 4, the test input data has a fixed resolution that is higher than the training data. From these results, we find that, when the training inputs have sufficiently high resolution (about  $20 \times 20$  or higher), our method achieves good accuracy independent of the test data, indicating its discretization independence. The discretization independence is further confirmed by the results in Table 2, which also shows consistent test errors among models trained and tested at sufficiently high resolutions (roughly  $R_1 \geq 23$  based on Table 2).

Figures 3 and 4 further show that significant errors occur at very low training resolutions, when the input lacks enough information to make an accurate prediction of the output. Interestingly, models trained on a very low resolution (e.g.  $R_1 = 8$ , or 13) datasets still capture some features of the operator. They are, however, heavily dependent on the particular training input resolution, as we see their predictions blow up completely when tested on a higher-resolution input in Figure 4. This is a result of the separate effects of a low-resolution input on the encoder and a low-resolution output on the reconstructor and loss function.

<sup>5</sup>We chose  $L^1$  loss because it seemed to give slightly better training results; however, we note that our results also hold if we use  $L^2$  or relative  $L^2$  loss, the most common alternatives.

<sup>6</sup>In all heat maps shown here and below, values exceeding the color bar range are marked in bright red (above range) and dark blue (below range).

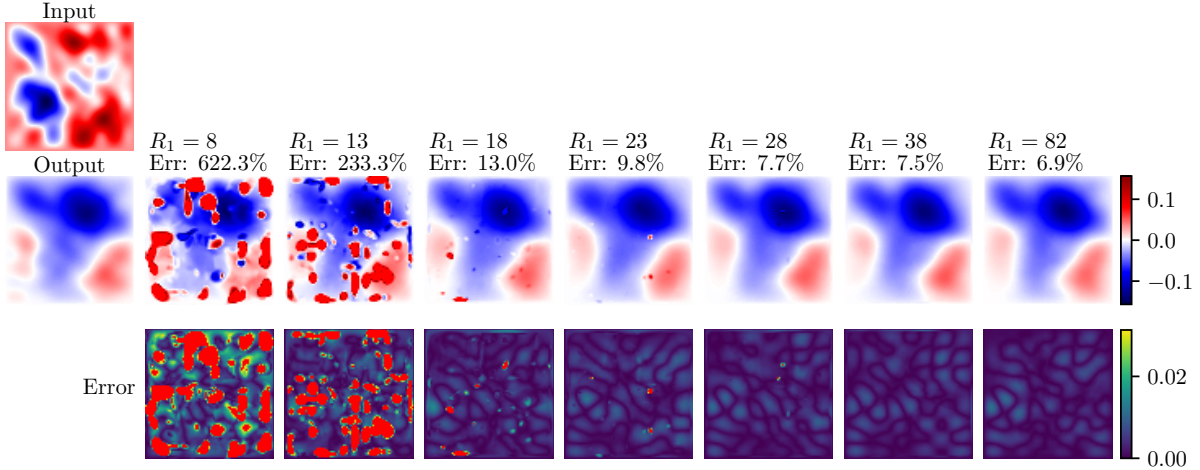


Figure 3: Effect of low-resolution **training outputs**. Sample predictions and errors of models with different training data resolutions<sup>6</sup>, with training resolution and relative  $L^1$  error above each prediction. Inputs are interpolated to the **same resolution used for training** in order to isolate the effect of the training output resolution.

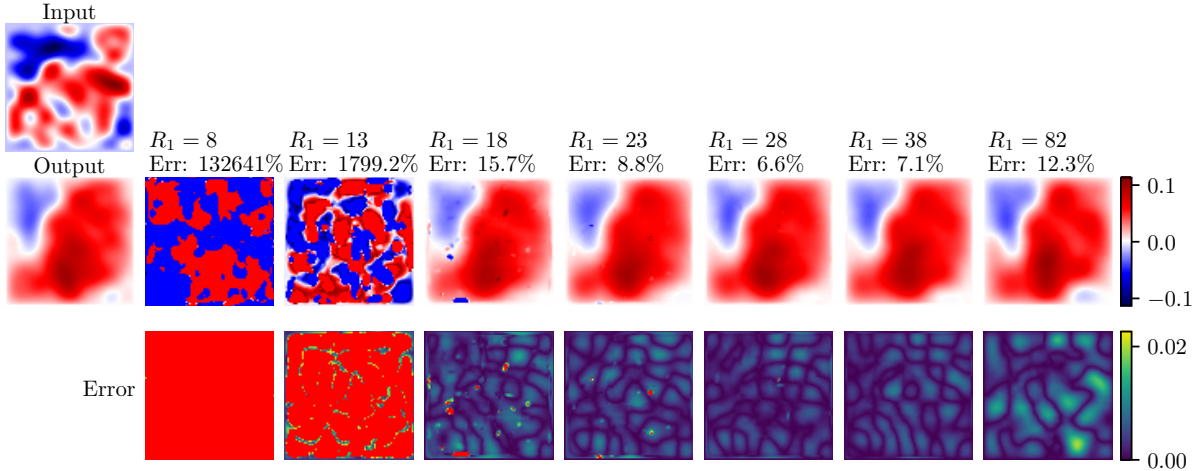


Figure 4: Effect of low-resolution **training inputs**. Sample predictions and errors of models with different training data resolutions for the fractional Poisson problem. All inputs have a **fixed high resolution (82)**, which highlights the effects of the input training resolution.

In Figure 3, by using test inputs with the same resolution as used in training, we isolate the effects of the low resolution of the output training data. Evidently, training with a low-resolution output results in predictions that are generally consistent with the true output, but with local blow-ups away from the output sampling points; see the red regions in the errors plot of Figure 3. On the other hand, we observe from Figure 4 that training with low resolution input data could lead to large global errors (see the red regions in the errors plot of Figure 4). Notably, the effects of low resolution input data appear to vanish at lower resolutions than the effects of low resolution output data; in particular, we can see that the model trained on data with resolution 18 (input and output) exhibits errors due to output resolution being too low (Figure 3) but no errors due to

input resolution being too low (Figure 4).

Testing resolution	Training resolution						
	8	13	18	23	28	38	82
8	6.9	1385.3	90.6	90.3	92.9	81.3	166.5
13	265253.6	7.9	14.4	12.2	12.2	11.7	12.2
18	260943.3	1218.0	8.5	10.3	9.7	9.9	10.6
23	265765.4	1620.5	18.6	9.5	8.5	8.7	9.1
28	263824.2	1437.7	21.5	9.8	8.1	8.2	9.1
38	263376.4	1525.0	21.2	11.1	8.6	8.4	8.6
82	259087.9	1466.6	20.4	10.8	8.8	8.6	8.5

Table 2: Relative  $L^1$  error (in %) for models trained and evaluated on single-fidelity datasets. Error is averaged across 8 training runs.

**Multifidelity training.** Our previous results show that our method can achieve discretization independence. Furthermore, training with low-resolution, single-fidelity data requires less training time but results in higher prediction errors. In contrast, training with high-resolution data leads to lower errors but incurs high computational costs. To leverage the advantages of both high and low resolutions, we conduct a second set of experiments that demonstrate that multifidelity training can not only improve training efficiency but also effectively eliminate the local blow-ups caused by low training output resolution.

Everything in these experiments is identical to the previous experiments, except that we use multifidelity training datasets with the same total size  $N$  as the single-fidelity training datasets used previously. Figure 5 presents the multifidelity training results, which may be compared with

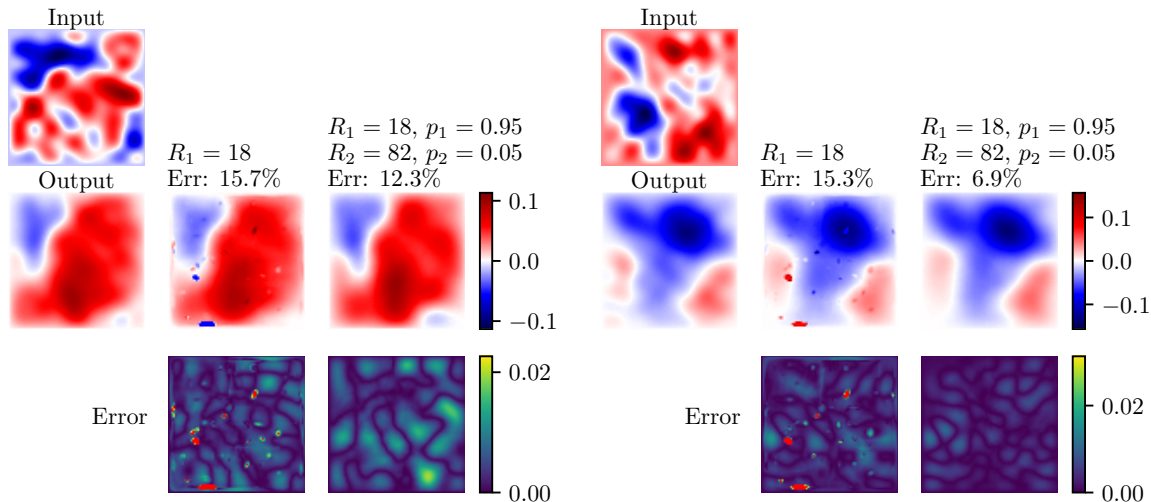


Figure 5: Multifidelity training reduces errors caused by low-resolution training outputs. Predictions and errors for models trained on low-fidelity and multifidelity training data, with training dataset parameters and relative  $L^1$  errors above each prediction. All test inputs share a fixed, high resolution (i.e. 82).

Figures 3–4. It shows that training with mostly low-fidelity data and even a small fraction (5%)

of high-fidelity data results in accuracy similar to models trained with all high-fidelity data and completely removes the artifacts caused by low output resolution. Furthermore, we see in Table 3 that error for models trained on multifidelity datasets is comparable to error for models trained on single-resolution, high-fidelity datasets, even if most of the data in the multifidelity dataset is lower-fidelity. This fact can result in simultaneously lower error and lower data costs.

Testing resolution	Training dataset parameters			
	$R_1 = 18$	$R_1 = 82$	$R_1 = 18, p_1 = 0.7$ $R_2 = 82, p_2 = 0.3$	$R_1 = 18, p_1 = 0.95$ $R_2 = 82, p_2 = 0.05$
13	14.4	12.2	9.7	9.4
18	8.5	10.6	8.2	7.9
38	21.2	8.6	7.6	8.2
82	20.4	8.5	7.5	7.9
Average data size	324	6724	2244	644

Table 3: Multifidelity training reduces error compared to single-fidelity training with a similar data cost. We report relative  $L^1$  errors (in %) for models trained on **both single- and multifidelity** datasets and evaluated on single-fidelity datasets. Error is averaged across 5 training runs. Average data size refers to the the average number of measurements used to represent a sample randomly chosen from the training dataset—data collection and training costs are proportional to average data size.

Indeed, for a two-dimensional problem such as this one, the average dimensions  $n$  and  $m$  of the discretized input and output spaces (i.e., the number of points at which the input and output functions are sampled) is given by

$$\mathbb{E}[m] = \mathbb{E}[n] = \sum_{i=1}^M p_i R_i^2. \quad (4.2)$$

Consequently, we see that the increased accuracy when  $R_1 = 82$  over  $R_1 = 18$  observed in Table 3 requires increasing data collection and training costs by a factor of around 20. In contrast, training with multifidelity data that includes only a small fraction of high-fidelity data can achieve the same increase in accuracy by increasing the data collection and training costs only by a factor of 2, a tenfold improvement over the single-fidelity approach.

## 4.2 Viscous Burgers' equation

In this section we learn the solution operator for nonlinear PDEs. Consider the one-dimensional viscous Burgers' equation with periodic boundary conditions:

$$\begin{cases} u_t(x, t) + \frac{1}{2}(u^2)_x = \nu u_{xx}, & x \in \Omega, \quad t \in (0, T], \\ u(x, 0) = u_0(x), & x \in \bar{\Omega}, \end{cases} \quad (4.3)$$

where the viscosity parameter  $\nu > 0$ . For a fixed viscosity  $\nu$ , the solution  $u(\cdot, T)$  at any time  $T > 0$  is determined by the initial condition  $u_0$ . Therefore, we can define an operator  $G^\dagger$  such that  $G^\dagger(u_0) = u(\cdot, T)$ . In our study, we choose  $\nu = 0.005$  and  $T = 1$ .

The training and testing data are generated by sampling the initial condition  $u_0(x)$  from a Gaussian process  $N(0, \sigma^2(-\Delta + \tau^2 I)^{-1})$  on  $\Omega$  with periodic boundary conditions [23]. In this case,

we choose  $\sigma = 5$  and  $\tau = 5$  and denote  $\Delta = \frac{d^2}{dx^2}$ . We then numerically solve (4.3) using a Fourier pseudospectral method for spatial discretization and the fourth-order Runge–Kutta method for time integration. Similar to section 4.1, we numerically solve the problem at high spatial resolution and then subsample both  $u_0(x)$  and  $u(x, T)$  at various lower spatial resolutions.

**Single-fidelity training.** We start with single-fidelity experiments, training models on various single-fidelity datasets and testing them at different resolutions. Figure 6 compares the predicted solutions with the ground truth solutions for three sample inputs, with models trained on single-fidelity datasets of different resolutions. It shows that the error is significantly exacerbated when

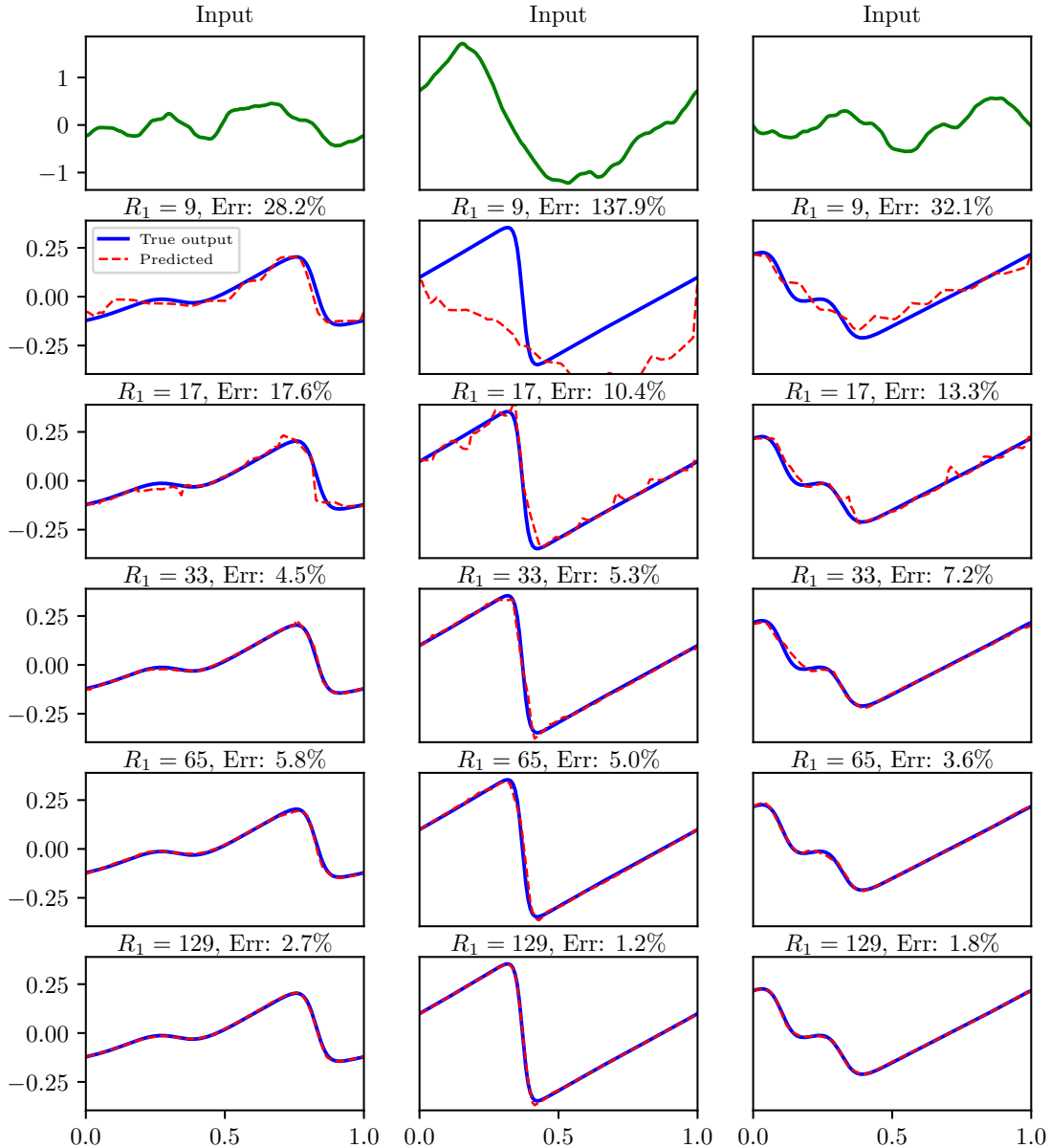


Figure 6: Sample predictions of models with different training data resolutions for the Burgers problem. All test inputs have the same high resolution (i.e. 129).

the training resolution is too low. For instance, when training with  $R_1 = 9$ , high errors are observed

in both the left and right examples, while the middle example experiences a blow-up. However, for sufficiently high-resolution training data, our method demonstrates empirical discretization independence, with consistent errors that are independent of the training and testing resolutions. This is further confirmed by the results presented in Table 4.

In Table 4, we summarize the average errors for models trained on single-fidelity datasets and tested on datasets with different resolutions. These testing resolutions are intentionally selected

Testing resolution	Training resolution										
	9	11	17	26	33	51	65	129	201	513	1025
9	1.7	174.1	1104.2	3063.0	4542.2	20759.4	18967.9	7237.3	5622.4	4766.3	1857.1
11	42.9	1.5	138.1	1044.2	2285.0	14163.1	11496.0	4282.8	2942.8	2481.8	787.0
17	33.4	77.5	1.7	67.1	97.7	1956.8	1811.1	478.9	275.9	205.8	40.6
26	39.1	58.4	21.3	3.2	12.7	123.0	151.5	30.6	15.1	26.0	14.1
33	42.3	74.4	14.0	11.4	3.2	12.6	13.9	6.6	11.3	11.1	6.4
51	41.0	62.2	20.0	6.8	10.9	3.2	10.1	9.4	4.0	10.5	9.4
65	46.2	80.4	16.8	11.0	10.2	9.4	3.4	3.5	8.8	4.5	3.6
129	46.7	81.7	17.3	11.1	6.8	9.3	3.7	3.2	8.8	3.5	3.3
201	41.1	63.4	19.6	7.3	10.9	4.0	9.7	9.1	3.2	9.0	9.0
401	41.1	63.3	19.6	7.3	10.9	4.0	9.7	9.1	3.2	9.0	9.0
513	46.8	81.9	17.6	11.1	6.2	9.4	3.7	3.3	8.8	3.4	3.2
1025	46.8	82.0	17.6	11.1	6.2	9.4	3.7	3.3	8.8	3.4	3.2

Table 4: Discretization independence and bias for Burgers problem. We present relative  $L^1$  testing errors (in %) for single-fidelity Burgers experiments. **Purple numbers** indicate that the test discretization and training discretization have **significantly overlapping sampling points** whereas white cells have almost no overlap.

to feature either many overlapping sample points or nearly disjoint sample points. For instance, the purple errors indicate that the training and testing resolutions share many identical sampling points, while the black errors indicate that the training and testing resolutions have almost no overlapping sampling points. Table 4 shows that while the test error remains consistent and acceptably low at sufficiently high training resolutions, there is a noticeable trend toward lower test error when the training and testing discretizations share many overlapping sample points. We call this effect *discretization bias*.

Table 4 further shows that, for a fixed training resolution, the error difference between two testing resolutions—one with many overlapping sample points and the other with no overlapping sampling points—remains roughly constant<sup>7</sup>. Hence, we propose the following metric to measure discretization bias, which we call the *performance gap*. Given a collection of single-fidelity testing datasets  $\mathcal{D}_1, \mathcal{D}_2, \dots, \mathcal{D}_K$ , let  $S_{\text{same}}$  be the set of indices of datasets whose sampling points highly overlap with those of one of the training discretizations, and let  $S_{\text{diff}}$  be the set of indices of the datasets whose sampling points do not. Then we define the performance gap as the difference in average testing error between test datasets with overlap and those without overlap:

$$g = \frac{1}{|S_{\text{same}}|} \sum_{j \in S_{\text{same}}} E_j - \frac{1}{|S_{\text{diff}}|} \sum_{j \in S_{\text{diff}}} E_j, \quad (4.4)$$

where  $E_j$  is the test error (in our case we use mean relative  $L^1$  error) on dataset  $\mathcal{D}_j$ . We note that the smaller the performance gap  $g$ , the more discretization-independent the model is. See more

<sup>7</sup>Assuming all have sufficiently high resolution to avoid low-resolution issues.

illustration and discussion in Table 6.

**Multifidelity training** Our studies of the Poisson problem show that multifidelity training can effectively reduce discretization dependence caused by low-resolution training outputs. Hence, we hypothesize that multifidelity training can also mitigate discretization bias. To test this, we conduct experiments by training models using multifidelity data, following the same setup used in Section 4.1 for multifidelity training. In this case, we specifically track which models are exposed to which sampling points in their training data. Consequently, we can compute the performance gap for selected models both from the single-fidelity experiments and also the performance gap for models with multifidelity training data.

In Table 5 we present the test errors for models trained on multifidelity datasets. The ta-

Testing resolution	Power /multiple	Training dataset parameters			
		$R_1 = 51, R_2 = 65$		$R_1 = 51, R_2 = 65, R_3 = 82$	
		Abs. error	Rel. error (%)	Abs. error	Rel. error (%)
26	5	1.49e-2	10.2	1.11e-2	7.3
28	3	1.47e-2	9.8	8.32e-3	5.2
33	2	7.73e-3	4.8	7.49e-3	4.6
50	7	1.09e-2	7.4	9.65e-3	6.4
51	10	6.40e-3	3.9	6.68e-3	4.1
65	2	6.50e-3	3.9	6.84e-3	4.1
82	3	1.14e-2	7.8	6.81e-3	4.1
126	5	1.11e-2	7.5	9.53e-3	6.3
129	2	6.74e-3	4.0	6.97e-3	4.2
201	10	6.87e-3	4.2	6.90e-3	4.2
244	3	1.14e-2	7.8	6.91e-3	4.2
344	7	1.08e-2	7.3	9.64e-3	6.4
401	10	6.88e-3	4.2	6.91e-3	4.2
513	2	6.77e-3	4.1	6.99e-3	4.2
626	5	1.11e-2	7.5	9.53e-3	6.3
730	3	1.14e-2	7.8	6.92e-3	4.2
1025	2	6.77e-3	4.1	6.99e-3	4.2

Table 5: Effect of multifidelity training on discretization bias. We report average errors across 10 runs of two models trained on multifidelity Burgers equation data with equal mixtures of discretizations (i.e.,  $p_i = \frac{1}{M}$ ). Each model used the same total amount of training data  $N$ , which was the same as in Table 4. **Purple numbers** indicate testing resolutions whose sampling points **significantly overlap** those of one of the training resolutions whereas white cells have almost no overlap. Resolutions with the same value in the Power/multiple column have significantly overlapping sampling points, and resolutions with different values have very few overlapping points.

ble shows that multifidelity training reduces error variability, with the more diverse multifidelity training data (i.e., more discretizations) leading to a more significant reduction. Importantly, more diverse multifidelity training reduces the error even for testing discretizations whose sampling points are not seen during training. This observation is further summarized in Table 6, which demonstrates clearly that increasing the diversity of the multifidelity training data reduces the performance gap, thus confirming our hypothesis that multifidelity training reduces discretization bias.

Training resolutions	Proportions	Performance gap
51	1	5.8
65	1	5.9
82	1	5.7
51, 65	$\frac{1}{2}, \frac{1}{2}$	3.5
51, 65, 82	$\frac{1}{3}, \frac{1}{3}, \frac{1}{3}$	2.2

Table 6: Discretization performance gap in relative  $L^1$  error (%) for models trained with different mixtures of training data—but still the same total amount of training data. Note that all models achieved roughly the same accuracy for resolutions whose sampling points were seen during training. Reported performance gap is the average over 10 runs.

Finally, it is important to note that discretization bias is not an inherently bad property. While it indicates that the model is mildly dependent on the discretization, this dependency manifests as an *increase* in accuracy on certain discretizations, surpassing the baseline accuracy on others (with the magnitude of the accuracy improvement quantified by the performance gap), as seen in Table 6.

### 4.3 Navier–Stokes problems

In this example we test our method on the Navier–Stokes equation. We again show that our method is discretization independent and further confirm, this time for a nonlinear problem, that multifidelity training effectively reduces errors due to low resolution training outputs, as demonstrated in the fractional Poisson example. Finally, we discuss a new phenomenon that arises when models trained on high-resolution data are tested on very low-resolution data.

We consider the two-dimensional incompressible Navier–Stokes equations for the vorticity  $\omega(x, y, t)$  with periodic boundary conditions, which are given by

$$\begin{cases} \omega_t + \mathbf{u} \cdot \nabla \omega = \nu \Delta \omega + f, & (x, y) \in \Omega, t \in (0, T], \\ \nabla \cdot \mathbf{u} = 0, & (x, y) \in \Omega, t \in (0, T], \\ \omega(x, y, 0) = \omega_0(x, y) & (x, y) \in \bar{\Omega}; \end{cases} \quad (4.5)$$

where  $\mathbf{u} = (u_1, u_2, 0)^T$  is the velocity, so that  $\nabla \times \mathbf{u} = (0, 0, \omega)^T$ . Note that the velocity  $\mathbf{u}$  can be obtained from  $\omega$  by finding a stream function  $\psi$ ; that is,  $\psi = \Delta \omega$ , subject to periodic boundary conditions. Then  $\mathbf{u}$  can be found by differentiation:  $\mathbf{u} = (\psi_y, -\psi_x, 0)^T$ . For a fixed viscosity value  $\nu > 0$ , the solution  $\omega(x, y, t)$  at a time  $t > 0$  is determined by the initial condition  $\omega_0$ . Thus, we define an operator  $G^\dagger$  by  $G^\dagger(\omega_0) = \omega(\cdot, \cdot, T)$ , where  $T > 0$  is a fixed final time. We aim to approximate this operator with viscosity  $\nu = 0.001$  and time  $T = 2.2$ .

The training and testing data are generated by sampling the initial condition  $\omega_0(x, y)$  from a Gaussian process  $N(0, \sigma^2(-\Delta + \tau^2)^{-\alpha/2})$  on  $\Omega$  with periodic boundary conditions. The parameters are chosen in all cases to be  $\alpha = 2.5$ ,  $\tau = 7$ , and  $\sigma = 7^{\frac{3}{4}}$ . We then solve (4.5) numerically for the solution  $\omega(x, y, T)$ , using the same numerical method and implementation as in [23]. Similarly, high resolution numerical solutions are obtained and subsampled to lower resolutions for model training.

**Single-fidelity training.** Once again, we train models with identical architectures on various single-fidelity datasets and then evaluate their performance on single-fidelity test datasets. The

results of these experiments are summarized in Table 7, in which we consistently observe discretization independence of our method at sufficiently high resolutions (e.g.  $R_1 > 33$ ). Sample results are

Testing resolution	Training resolution					
	16	17	28	33	46	65
9	6521.7	17.3	24.6	23.2	22.6	22.0
16	10.6	32.8	15.8	12.9	12.4	12.0
17	780.8	11.9	15.5	12.6	11.9	11.7
28	64243.1	40.4	14.1	11.8	10.9	10.9
33	16426.6	46.8	14.6	11.6	10.8	10.8
46	24168.8	40.4	15.0	12.0	10.8	10.9
65	26430.4	40.4	14.6	11.7	10.6	10.7
129	17828.0	40.7	14.9	12.0	11.0	10.9
136	16727.9	40.5	14.9	11.8	10.8	10.8

Table 7: Relative  $L^1$  error (in %) for models trained and evaluated on single-fidelity datasets. Median error (in this problem there were a few significant outliers that caused the mean to be an unreliable measure) is averaged across 8 training runs.

visualized in Figure 7, which further indicates the discretization independence of our method and shows that the same low-resolution effects from the fractional Poisson problem are also present in the Navier–Stokes problem.

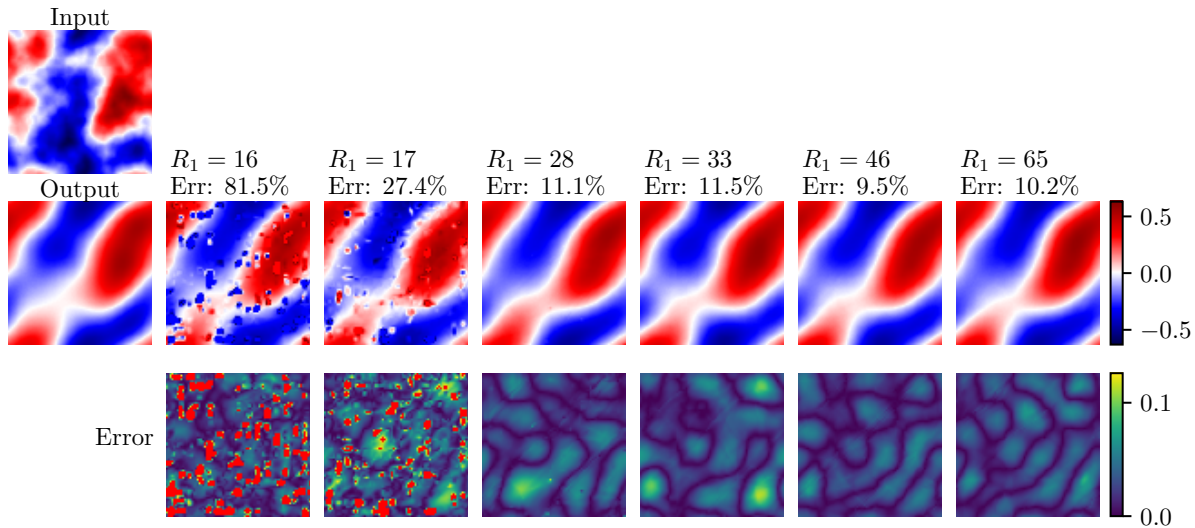


Figure 7: Effect of low-resolution **training outputs**. Sample predictions and errors of models with different training data resolutions, with training resolution and relative  $L^1$  error above each prediction. Inputs are interpolated to the **same resolution used for training**.

Moreover, our experiments show that if *test* data with too low a resolution is used—rather than training data with too low resolution— then all models will have higher error if they were trained at a different resolution, even if the training resolutions were high. This phenomenon can be seen in Table 7 and is further demonstrated in Figure 8, in which we observe that testing with low-resolution

inputs introduces larger errors for models trained on different resolution inputs. This again suggests that very low-resolution inputs lack sufficient information to make accurate predictions.

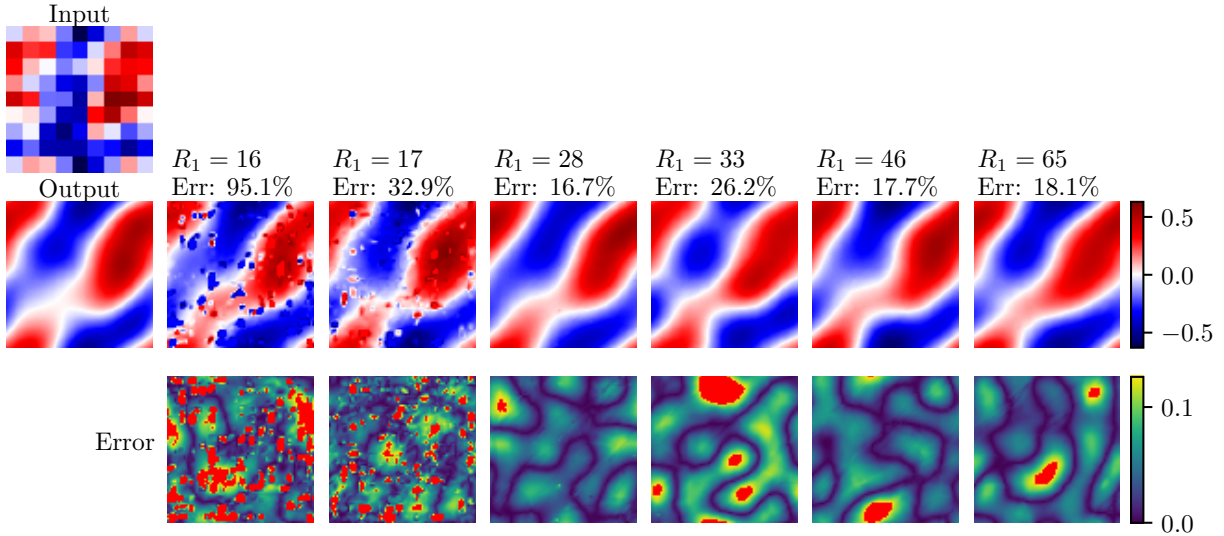


Figure 8: Effect of low-resolution **test input**. Sample predictions and errors of models with different training data resolutions. All inputs have a **fixed low resolution** (i.e. 9), which highlights the effects of the input testing resolution.

**Multifidelity training** We conduct similar multifidelity experiments to those for the fractional Poisson example. As shown in Figure 9, we observe that multifidelity training with even a small fraction of high-fidelity data yields the same benefits in this problem as it did in the fractional Poisson problem. Specifically, it eliminates the localized errors caused by training with low-resolution data without incurring the significantly greater costs of training with only high-fidelity data.

In Table 8, we further analyze the effect of multifidelity training on reducing error and discretization bias. Comparing the single-fidelity case with  $R_1 = 17$  to the multifidelity case with  $R_1 = 17$ ,  $p_1 = 0.95$  and  $R_2 = 65$ ,  $p_2 = 0.05$  in Table 8 suggests that multifidelity training even with a small fraction of high-resolution data significantly reduces error due to output resolution being too low. On the other hand, discretization bias seems to be negligible in this problem, as the performance gap is nearly zero for all training datasets. As shown in Table 8, the performance gap is less than 0.1% regardless of the training dataset.

## 5 Conclusion and discussion

In this paper we presented new concepts of numerical operator learning and discretization independence. Based on these concepts, we proposed a novel encode-approximate-reconstruct model, about which we proved approximation guarantees using established theory for these types of models while retaining discretization independence, which existing methods do not. Our experiments showed that our method is empirically discretization independent on a diverse set of operators. We were also able to observe phenomena related to multifidelity data; namely, we observed three types of low-resolution breakdowns, due to training inputs, training outputs, and testing inputs.

Furthermore, we demonstrated that our model can leverage multifidelity data to reduce low-resolution breakdowns and achieve good accuracy with lower data costs. By establishing an un-

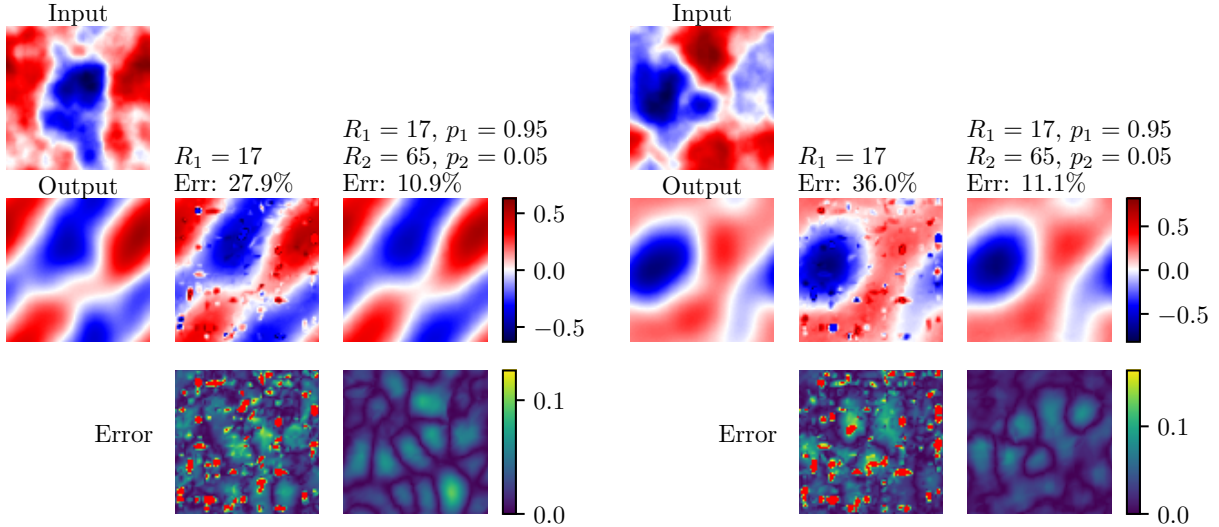


Figure 9: Multifidelity training reduces errors caused by low-resolution training outputs. Predictions and errors for models trained on low-fidelity and multifidelity training data, with training dataset parameters and relative  $L^1$  errors above each prediction. All test inputs share a fixed, high resolution (i.e. 65).

Testing resolution	Training dataset parameters			
	$R_1 = 17$	$R_1 = 65$	$R_1 = 17, p_1 = 0.7$ $R_2 = 65, p_2 = 0.3$	$R_1 = 17, p_1 = 0.95$ $R_2 = 65, p_2 = 0.05$
28	40.4	10.9	11.3	12.1
33	46.8	10.8	11.2	12.1
46	40.4	10.7	11.4	12.2
129	40.7	10.9	11.6	12.4
Performance gap	0.02	0.06	-0.03	0.00
Average data size	289	4225	1470	486

Table 8: Multifidelity training reduces error compared to single-fidelity training with a similar data cost. We report relative  $L^1$  errors (in %) and performance gaps (for test  $R_1 \geq 28$ ) for models trained on **both single- and multifidelity** datasets and evaluated on single-fidelity datasets. Error and performance gap are averaged across 8 training runs. Average data size refers to the the average number of measurements used to represent a sample randomly chosen from the training dataset—data collection and training costs are proportional to average data size.

Understanding of how low-fidelity data introduces error, we were able to show with our experiments that multifidelity training can reduce some types of error caused by low-fidelity training data, enabling faster training with lower-fidelity datasets. Additionally, we observed the new phenomenon of discretization bias in the case of the Burgers example, and we showed how multifidelity training mitigates it.

**Acknowledgments** This work was partially supported by the Missouri University of Science and Technology’s Kummer Institute for Student Success, Research, and Economic Development

through the Kummer Innovation and Entrepreneurship Doctoral Fellowship.

## References

- [1] Alkin, B., Fürst, A., Schmid, S. L., Gruber, L., Holzleitner, M., and Brandstetter, J. Universal physics transformers: A framework for efficiently scaling neural operators. In *the 38th Annual Conference on Neural Information Processing Systems*. 2024.
- [2] Bartolucci, F., de Bezenac, E., Raonic, B., Molinaro, R., Mishra, S., and Alaifari, R. Representation equivalent neural operators: A framework for alias-free operator learning. In *the 37th Conference on Neural Information Processing Systems*. 2023.
- [3] Berner, J., Grohs, P., Kutyniok, G., and Petersen, P. Chapter 1 - The Modern Mathematics of Deep Learning. In *Mathematical Aspects of Deep Learning*, pp. 1–111. Cambridge University Press, 2022.
- [4] Bhattacharya, K., Hosseini, B., Kovachki, N. B., and Stuart, A. M. Model reduction and neural networks for parametric PDEs. *SMAI J. Comp. Math.*, 7:121–157, 2021.
- [5] Cao, S. Choose a transformer: Fourier or Galerkin. In *Advances in Neural Information Processing Systems*, vol. 34. 2021.
- [6] Chen, T. and Chen, H. Universal approximation to nonlinear operators by neural networks with arbitrary activation functions and its application to dynamical systems. *IEEE Trans. Neural Netw.*, 6(4):911–917, 1995.
- [7] Choubineh, A., Chen, J., Wood, D. A., Coenen, F., and Ma, F. Fourier neural operator for fluid flow in small-shape 2D simulated porous media dataset. *Algorithms*, 16(1):24, 2023.
- [8] De, S., Reynolds, M., Hassanaly, M., King, R. N., and Doostan, A. Bi-fidelity modeling of uncertain and partially unknown systems using DeepONets. *Comput. Mech.*, 71(6):1251–1267, 2023.
- [9] Duo, S., van Wyk, H. W., and Zhang, Y. A novel and accurate finite difference method for the fractional Laplacian and the fractional Poisson problem. *J. Comput. Phys.*, 355:233–252, 2018.
- [10] Fernández-Godino, M. G. Review of multi-fidelity models. *Adv. Comput. Sci. Eng.*, 1(4):351–400, 2023.
- [11] Fonseca, A. H. D. O., Zappala, E., Caro, J. O., and Dijk, D. V. Continuous spatiotemporal transformer. In *Proceedings of the 40th International Conference on Machine Learning*, pp. 7343–7365. 2023.
- [12] Goswami, S., Bora, A., Yu, Y., and Karniadakis, G. E. Physics-Informed Deep Neural Operator Networks. In *Machine Learning in Modeling and Simulation: Methods and Applications*, pp. 219–254. Springer International Publishing, 2023.
- [13] Hao, Z., Wang, Z., Su, H., Ying, C., Dong, Y., Liu, S., Cheng, Z., Song, J., and Zhu, J. GNOT: A general neural operator transformer for operator learning. In *Proceedings of the 40th International Conference on Machine Learning*, pp. 12556–12569. 2023.

- [14] Hesthaven, J. and Ubbiali, S. Non-intrusive reduced order modeling of nonlinear problems using neural networks. *J. Comput. Phys.*, 363:55–78, 2018.
- [15] Howard, A. A., Perego, M., Karniadakis, G. E., and Stinis, P. Multifidelity deep operator networks for data-driven and physics-informed problems. *J. Comput. Phys.*, 493:112462, 2023.
- [16] Kingma, D. P. and Ba, J. Adam: A method for stochastic optimization. In *the 3rd International Conference on Learning Representations*. 2015.
- [17] Kissas, G., Seidman, J., Guilhoto, L. F., Preciado, V. M., Pappas, G. J., and Perdikaris, P. Learning operators with coupled attention. *J. Mach. Learn. Res.*, 23:1–63, 2022.
- [18] Kovachki, N., Li, Z., Liu, B., Azizzadenesheli, K., Bhattacharya, K., Stuart, A., and Anandkumar, A. Neural operator: Learning maps between function spaces with applications to PDEs. *J. Mach. Learn. Res.*, 24(1):1–97, 2024.
- [19] Kovachki, N. B., Lanthaler, S., and Mishra, S. On universal approximation and error bounds for Fourier Neural Operators. *J. Mach. Learn. Res.*, 22:1–76, 2021.
- [20] Kovachki, N. B., Lanthaler, S., and Stuart, A. M. Chapter 9 - Operator Learning: Algorithms and Analysis. In *Numerical Analysis Meets Machine Learning*, vol. 25 of *Handbook of Numerical Analysis*, pp. 419–467. 2024.
- [21] Lanthaler, S., Mishra, S., and Karniadakis, G. E. Error estimates for DeepONets: A deep learning framework in infinite dimensions. *Trans. Math. Appl.*, 6(1):tnac001, 2022.
- [22] Li, Z., Kovachki, N., Azizzadenesheli, K., Liu, B., Stuart, A., Bhattacharya, K., and Anandkumar, A. Multipole graph neural operator for parametric partial differential equations. In *Advances in Neural Information Processing Systems*, vol. 33, pp. 6755–6766. 2020.
- [23] Li, Z., Kovachki, N. B., Azizzadenesheli, K., Liu, B., Bhattacharya, K., Stuart, A., and Anandkumar, A. Fourier neural operator for parametric partial differential equations. In *International Conference on Learning Representations*. 2021.
- [24] Li, Z., Kovachki, N. B., Choy, C., Li, B., Kossaifi, J., Otta, S. P., Nabian, M. A., Stadler, M., Hundt, C., Azizzadenesheli, K., and Anandkumar, A. Geometry-informed neural operator for large-scale 3D PDEs. In *the 37th Conference on Neural Information Processing Systems*. 2023.
- [25] Li, Z., Meidani, K., and Farimani, A. B. Transformer for partial differential equations’ operator learning. *Trans. Mach. Learn.*, 2023.
- [26] Li, Z., Peng, W., Yuan, Z., and Wang, J. Fourier neural operator approach to large eddy simulation of three-dimensional turbulence. *Theor. Appl. Mech. Lett.*, 12(6):100389, 2022.
- [27] Li, Z., Shu, D., and Farimani, A. B. Scalable transformer for PDE surrogate modeling. In *the 37th Conference on Neural Information Processing Systems*. 2023.
- [28] Lu, L., Jin, P., and Karniadakis, G. E. DeepONet: Learning nonlinear operators for identifying differential equations based on the universal approximation theorem of operators. *Nat. Mach. Intell.*, 3(3):218–229, 2021.
- [29] Lu, L., Meng, X., Cai, S., Mao, Z., Goswami, S., Zhang, Z., and Karniadakis, G. E. A comprehensive and fair comparison of two neural operators (with practical extensions) based on FAIR data. *Comput. Methods Appl. Mech. Eng.*, 393:114778, 2022.

- [30] Lu, L., Pestourie, R., Johnson, S. G., and Romano, G. Multifidelity deep neural operators for efficient learning of partial differential equations with application to fast inverse design of nanoscale heat transport. *Phys. Rev. Res.*, 4(2):023210, 2022.
- [31] Ovadia, O., Kahana, A., Stinis, P., Turkel, E., Givoli, D., and Karniadakis, G. E. ViTO: Vision transformer-operator. *Comput. Methods Appl. Mech. Eng.*, 428:117109, 2024.
- [32] Paszke, A., Gross, S., Massa, F., Lerer, A., Bradbury, J., Chanan, G., Killeen, T., Lin, Z., Gimelshein, N., Antiga, L., Desmaison, A., Kopf, A., Yang, E., DeVito, Z., Raison, M., Tejani, A., Chilamkurthy, S., Steiner, B., Fang, L., Bai, J., and Chintala, S. Pytorch: An imperative style, high-performance deep learning library. In *Advances in Neural Information Processing Systems 32*, pp. 8024–8035. 2019.
- [33] Prasthofer, M., De Ryck, T., and Mishra, S. Variable-input deep operator networks, 2022.
- [34] Raonic, B., Molinaro, R., Ryck, T. D., Rohner, T., Bartolucci, F., Alaifari, R., Mishra, S., and de Bezenac, E. Convolutional neural operators for robust and accurate learning of PDEs. In *the 37th Conference on Neural Information Processing Systems*. 2023.
- [35] Ros-Oton, X. and Serra, J. The Dirichlet problem for the fractional Laplacian: regularity up to the boundary. *J. Math. Pures Appl. (9)*, 101(3):275–302, 2014.
- [36] Sun, Y., Moya, C., Lin, G., and Yue, M. DeepGraphONet: A deep graph operator network to learn and zero-shot transfer the dynamic response of networked systems. *IEEE Syst. J.*, 17(3):4360–4370, 2023.
- [37] Tanyu, D. N., Ning, J., Freudenberg, T., Heilenkötter, N., Rademacher, A., Iben, U., and Maass, P. Deep learning methods for partial differential equations and related parameter identification problems. *Inverse Probl.*, 39(10):103001, 2023.
- [38] Thakur, A., Tripura, T., and Chakraborty, S. Multi-fidelity wavelet neural operator with application to uncertainty quantification. *Preprint*, 2022.
- [39] Wen, G., Li, Z., Azizzadenesheli, K., Anandkumar, A., and Benson, S. M. U-FNO – An enhanced Fourier neural operator-based deep-learning model for multiphase flow. *Adv. Water Resour.*, 163:104180, 2022.
- [40] Zhou, S. and Zhang, Y. A novel and simple spectral method for nonlocal PDEs with the fractional Laplacian. *Comput. Math. Appl.*, 168:133–147, 2024.

# Appendix

## A Notation

Symbol	Meaning
$d_U$	Dimension of the <b>input</b> function domain
$d_V$	Dimension of the <b>output</b> function domain
$\Omega_U \subseteq \mathbb{R}^{d_U}$	The domain of the <b>input</b> functions
$\Omega_V \subseteq \mathbb{R}^{d_V}$	The domain of the <b>output</b> functions
$\mathcal{U} \subseteq L^2(\Omega_U)$	Vector space of <b>input</b> functions
$\mathcal{V} \subseteq L^2(\Omega_V)$	Vector space of <b>output</b> functions
$u \in \mathcal{U}$	<b>Input</b> function
$v \in \mathcal{V}$	<b>Output</b> function
$m$	Dimension of the <b>input</b> discretized space
$n$	Dimension of the <b>output</b> discretized space
$D_U : \mathcal{U} \rightarrow \mathbb{R}^m$	Discretization of the <b>input</b> space
$D_V : \mathcal{V} \rightarrow \mathbb{R}^n$	Discretization of the <b>output</b> space
$\mathbf{u} = D_U(u) \in \mathbb{R}^m$	Discrete representation of <b>input</b> function
$\mathbf{v} = D_V(v) \in \mathbb{R}^n$	Discrete representation of <b>output</b> function
$G^\dagger : \mathcal{U} \rightarrow \mathcal{V}$	True operator that is to be learned
$G_\theta : \mathcal{U} \rightarrow \mathcal{V}$	Parametric model for $G^\dagger$ with parameters $\theta \in \mathbb{R}^P$
$\tilde{G}_\theta(D_U, D_V; \cdot) : \mathbb{R}^m \rightarrow \mathbb{R}^n$	The numerical implementation of $G_\theta$ .
$p$	Dimension of <b>input</b> latent space (before approximator)
$q$	Dimension of <b>output</b> latent space (after approximator)
$E : \mathcal{U} \rightarrow \mathbb{R}^p$	<b>Encoder</b> module
$A : \mathbb{R}^p \rightarrow \mathbb{R}^q$	<b>Approximator</b> module
$R : \mathbb{R}^q \rightarrow \mathcal{V}$	<b>Reconstructor</b> module
$\theta_E$	<b>Encoder</b> parameters
$\theta_A$	<b>Approximator</b> parameters
$\theta_R$	<b>Reconstructor</b> parameters
$\Phi^E : \mathbb{R}^{d_U} \rightarrow \mathbb{R}^p$	<b>Encoder</b> basis network
$\Phi^A : \mathbb{R}^p \rightarrow \mathbb{R}^q$	<b>Approximator</b> neural network
$\Phi^R : \mathbb{R}^{d_V} \rightarrow \mathbb{R}^q$	<b>Reconstructor</b> basis network

Table 9: Summary of notations used in the paper.

## B Training details

Here we provide details related to the numerical experiments that were omitted from Section 4. All training code was implemented in PyTorch [32] and run on an NVIDIA GeForce RTX 4070 Ti GPU with 12GB of video memory.

**Model architectures:** As mentioned in Section 4, we use the same model architecture for all training runs of a particular PDE problem; however, we used slightly different architectures for each problem. In all cases, we implemented each neural network in our model with a multilayer

perceptron with Leaky ReLU activation function with a slope of 0.03; network architectures are presented in Table 10.

Problem	Network	Input	Hidden Layers	Output
Fractional Poisson	$\Phi^E$	290	$128 \times 3$	96
	$\Phi^A$	96	$256 \times 2$	96
	$\Phi^R$	290	$128 \times 3$	96
Burgers	$\Phi^E$	26	$96 \times 3$	18
	$\Phi^A$	18	$128 \times 4$	18
	$\Phi^R$	26	$96 \times 3$	18
Navier–Stokes	$\Phi^E$	202	$128 \times 3$	96
	$\Phi^A$	96	$256 \times 4$	96
	$\Phi^R$	202	$128 \times 3$	96

Table 10: All neural network architectures used in our models (number of neurons in each layer; for hidden layers, number of neurons  $\times$  number of layers).

Additionally, we use Fourier feature expansion following a similar implementation to that of Lu et al. for DeepONet [29]. The number of modes in each spatial direction are given in Table 11; the need to take these extra features as input is why the the encoder and reconstructor networks have a different number of input neurons from the expected  $d_U$  and  $d_V$ .

Problem	Network	Modes
Fractional Poisson	$\Phi^E$	12
	$\Phi^R$	12
Burgers	$\Phi^E$	12
	$\Phi^R$	12
Navier–Stokes	$\Phi^E$	10
	$\Phi^R$	10

Table 11: Number of Fourier feature expansion modes in all models.

**Training hyperparameters:** To train our models we used the Adam [16] optimizer with momentum parameters  $\beta_1 = 0.9$  and  $\beta_2 = 0.999$  (defaults in PyTorch [32]) and a batch size of 10 for all problems. We chose different values of the following hyperparameters for each problem: the initial learning rate  $\eta_0$ , the geometric learning rate decay factor  $\gamma$ , and the total number of training epochs  $N_e$ . The values used on each problem are presented in Table 12. These values were chosen through preliminary experiments to balance performance and training cost.

Problem	$\eta_0$	$\gamma$	$N_e$
Fractional Poisson	0.003	0.9995	2000
Burgers	0.005	0.9970	1000
Navier–Stokes	0.003	0.9990	750

Table 12: Training hyperparameters by problem. Recall that the total training data size is  $N = 2048$  for fractional Poisson and Burgers models and  $N = 4096$  for Navier–Stokes models, which is why fewer epochs are needed for the Navier–Stokes problem.